Wei Gao, Yuki Shimizu
Optical Metrology for Precision Engineering

Also of Interest

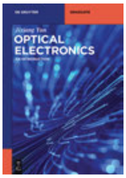

Optical Electronics.
An Introduction
Jixiang Yan, 2019
ISBN 978-3-11-050049-3, e-ISBN (PDF) 978-3-11-050060-8
e-ISBN (EPUB) 978-3-11-049800-4

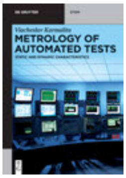

Metrology of Automated Tests.
Static and Dynamic Characteristics
Viacheslav Karmalita, 2020
ISBN 978-3-11-066664-9, e-ISBN (PDF) 978-3-11-066667-0,
e-ISBN (EPUB) 978-3-11-066669-4

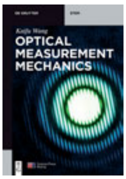

Optical Measurement Mechanics
Kaifu Wang, 2018
ISBN 978-3-11-057304-6, e-ISBN (PDF) 978-3-11-057305-3,
e-ISBN (EPUB) 978-3-11-057320-6

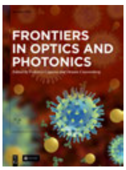

Frontiers in Optics and Photonics
Federico Capasso, Dennis Couwenberg (Eds.), 2021
ISBN 978-3-11-070973-5, e-ISBN (PDF) 978-3-11-071068-7,
e-ISBN (EPUB) 978-3-11-071070-0

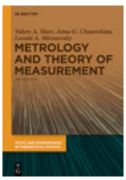

Metrology and Theory of Measurement
Valery A. Slaev, Anna G. Chunovkina, Leonid A. Mironovsky, 2020
ISBN 978-3-11-065094-5, e-ISBN (PDF) 978-3-11-065250-5,
e-ISBN (EPUB) 978-3-11-065131-7

Wei Gao, Yuki Shimizu

Optical Metrology for Precision Engineering

DE GRUYTER

Authors
Prof. Wei Gao
Department of Finemechanics
Graduate School of Engineering
Tohoku University
6-6-01 Aramaki Aza aoba
Sendai
980-8579
Japan
i.ko.c2@tohoku.ac.jp

Prof. Yuki Shimizu
Department of Finemechanics
Graduate School of Engineering
Tohoku University
6-6-01 Aramaki Aza Aoba
Sendai
980-8579
Japan
yuki.shimizu.d2@tohoku.ac.jp

ISBN 978-3-11-054109-0
e-ISBN (PDF) 978-3-11-054236-3
e-ISBN (EPUB) 978-3-11-054127-4

Library of Congress Control Number: 2021943619

Bibliographic information published by the Deutsche Nationalbibliothek
The Deutsche Nationalbibliothek lists this publication in the Deutsche Nationalbibliografie; detailed bibliographic data are available on the Internet at http://dnb.dnb.de.

Cover image: Wei Gao
Typesetting: Integra Software Services Pvt. Ltd.
Printing and binding: CPI books GmbH, Leck

www.degruyter.com

Preface

Precision engineering is a discipline to develop and apply principles of design, manufacture, control and measurement for precision machines and precision manufacturing. Precision metrology, often called dimensional metrology, is one of the cornerstones to support precision engineering. It is the science and technology of measurement for quantifying physical quantities derived from the SI base quantities of length and time, including geometrical properties of an object such as length, angle and surface topography, as well as kinematic properties such as displacement, velocity and acceleration. A high degree of precision and a low degree of uncertainty are required for such a measurement. Precision metrology is particularly important for modern manufacturing industries based on mass production of interchangeable parts by using various machine tools. The concept of interchangeability has been the greatest achievement of the twentieth century, which has substantially changed not only the ways of manufacturing but also the lifestyles of human beings. In interchangeable manufacturing, the parts are required to be made to the designed geometrical specifications so that the parts made in different places by different operators can be exchangeable with each other for efficient assembly of new products and easy repair of existing products. This can only be made possible when the necessary level of quality control is established in the manufacturing processes based on precision measurements of the geometrical specifications of the manufactured parts. Precision measurement of the kinematic properties of machine tools is also essential for supporting the interchangeable manufacturing.

On the other hand, light has long been utilized in measurement activities of human history. Optical measurement technologies have evolved to an independent branch of metrology called optical metrology. Optical metrology can be applied for measurement of almost all kinds of physical quantities, including the SI base quantities of time, length, mass, temperature, luminous intensity and their derived quantities. Noncontact, fast and sensitive are some of the important features of optical metrology. Optical measurement technologies are playing an increasingly important role in precision metrology where accurate measurements are required to be made in a short time and with minimal influence on the measurement target.

This book presents the state-of-the-art optical technologies of dimensional metrology for precision engineering. This book is composed of 12 chapters. The manuscripts of Chapters 1–5, 7–9 and 11 were mainly written by Wei Gao and the rest were written by Yuki Shimizu. Yuki Shimizu also prepared most of the figures and made the final edition of the entire book. The first half of the book, from Chapters 1 to 6, presents optical sensors and systems with conventional continuous-wave laser source. Optical sensors for the measurement of angular and translational displacements, which are fundamental quantities in precision metrology, are presented in Chapters 1–4. Chapter 1 describes optical angle sensors based on laser autocollimation, which can make nanoradian angle measurement while maintaining a compact

https://doi.org/10.1515/9783110542363-202

sensor size. The angle sensor is then expanded for three-axis measurement by using a refraction grating as the target reflector in Chapter 2. In Chapters 3 and 4, surface encoders are presented for XY, XYZ or Z–θ_Z multi-axis motion measurement by using grating scales. A concept of mosaic surface encoder is also presented for expansion of the measurement range. Chapter 5 presents a number of unique optical scanning profilers for surface topographic measurement under in-line and/or on-machine conditions. In Chapter 6, fabrication of grating scales by interference lithography is presented together with fast and accurate calibration technologies. The second half of the book, from Chapters 7 to 12, presents the next-generation optical measurement technologies based on ultrashort pulse laser and optical frequency comb. Ultrashort pulse laser angle sensing methods are presented in Chapter 7 by taking use of the unique characteristics of ultrashort pulses, including second-harmonic generation. Chapter 8 provides a mathematical analysis on the optical frequency comb, where the theorem of Fourier transform, including Fourier integral and Fourier series, is applied to analyze the relationship between a train of ultrashort pulses and the optical frequency comb as well as to reveal the key features of optical frequency comb. Chapters 9 to 12 present optical sensors based on optical frequency comb; an angle comb for absolute angle measurement, a chromatic confocal comb for absolute displacement measurement, a position comb for absolute position measurement, and applied comb metrology including a comb surface profiler.

I wish that this book can provide the newest information on the advancement in optical dimensional metrology to engineers in areas of precision engineering, optical engineering, mechanical engineering and nanotechnology, as well as the postgraduate and undergraduate students learning in these fields. I sincerely wish that this book could inspire research fellows and postgraduate students to create new ideas in dimensional metrology, especially in the next-generation measurement technologies based on optical frequency comb and ultrashort optical pulses.

This book is the record of an important part of the research work that the authors have been involved in for over the past decade. I would like to thank my colleagues and many students in the Precision Nanometrology Laboratory for their significant contributions to the development of the technologies presented in this book. Hiraku Matsukuma, So Ito, Yuanliu Chen, Xiuguo Chen, Akihide kimura, Yusuke Saito, Takemi Asai, WooJae Kim, SungHo Jang, Xinghui Li, Zengyuan Niu, Xin Xiong, Chong Chen, Lue Quan, Wijayanti Dwi Astuti, Dong Wook Shin, Kentaro Uehara, Shinji Sato, Haemin Choi, Kouji Hosono, Hiroshi Muto, Shinichi Osawa, Takeshi Ito, Dai Murata, Tatsuya Ishikawa, Yukitoshi Kudo, Ryo Aihara, Taiji Maruyama, Masaya Furuta, Jun Tamada, Taku Nakamura, Shaoqing Yang, Zongwei Ren, Shuhe Madokoro, Kazuki Mano, Ryo Ishizuka, Yuri Kanda, Ryo Sato and Shota Takazono are some of them. Mr. Ryo Sato carefully checked and revised Chapters 8 and 11. Prof. Hiraku Matsukuma also made comments to these two chapters. I would like to thank Ms. Karolina Sobańska, Ms. Cruz-Kaciak Aneta, Mr. Leonardo Milla, Ms. Chao Yang, Mr. Joachim Katzmarek and other staffs of De Gruyter for their dedicated efforts that have made this book possible. The financial support from the Japan Society for Promotion of Science is also appreciated. Special thanks to Dr. Hajime Inaba, Head of Optical Frequency Measurement Group, National Metrology Institute of Japan, AIST, for his invaluable advice on the development of the fiber-based frequency comb system in Chapter 11. The invaluable advice from Prof. Lijiang Zeng, Tsinghua University on grating fabrication is also appreciated.

I wish to express my thanks to my wife, Hong Shen, for her warm support. The same appreciation also goes to Mrs. Yayoi Shimizu, Prof. Yuki Shimizu's wife, for her support to her husband. This book was written in a difficult situation of COVID-19. It would never have been completed without the patience, sacrifice, encouragement and support from the two families. Finally, I would like to thank my co-author, Prof. Yuki Shimizu, for his hardworking on this book as well as his great contribution to the development of the measurement technologies presented in this book.

Wei Gao
Sendai, Japan
March, 2021

Contents

Chapter 1
Laser autocollimator

1.1 Introduction

A precision linear motion slide is an important element in precision engineering. It is used to generate precision linear motions in machine tools and scanning-type measuring instruments [1, 2]. A linear motion slide, which is often called a linear slide or a linear stage, is composed of a moving table and a straight guideway. A moving table is sometimes called a carriage or a saddle, and a straight guideway is often referred to as a rail. In a linear slide, the carriage is moved to a command position along a straight line. The line is referred to as the axis of motion of the carriage (X-axis). The closeness of the command position to the actual position of the carriage is called the positioning accuracy. On the other hand, the closeness of the actual path of the carriage movement to the X-axis is referred to as the straightness motion accuracy. Many precision linear slides are required to have sub-micrometric positioning accuracy and straightness motion accuracy [3].

For slide precision positioning, it is necessary to make closed-loop feedback control of the slide carriage by using the result of position measurement with an accurate position sensor, which is often a linear encoder [4]. With the advances in sensor technologies, sub-micrometric or even nanometric precision positioning of the slide carried has been realized [5]. On the other hand, the straightness motion accuracy is mainly determined by the form accuracy of slide guideways. A pair of parallel guideways is typically employed in a linear slide to provide physical constraints to the slide carriage in the directions vertical to the axis of motion of the carriage [6]. Any flatness errors in the surface form of each guideway will cause corresponding out-of-straightness motion errors of the slide carriage [7]. The flatness error of the guideway surface can also generate tilt motion errors of the slide carriage. For obtaining sub-micrometric straightness motion accuracy, it is necessary to machine the guideways with sub-micrometric flatness accuracy. In addition, it is also necessary to identify the tilt motion accuracy after the carriage is assembled with the guideways.

As shown in Fig. 1.1, not only the tilt motion accuracy of the slide carriage but also the flatness of the slide guideway can be measured by an autocollimator. In the machining process, the slide guideway is first ground by a grinding machine to a flatness on the order of several micrometers [8, 9]. To further reduce the flatness error to sub-micrometer level, a hand scraping operation is carried out. Although such an operation is time-consuming and highly dependent on the skill of the operator, it is effective to improve the guideway flatness beyond the machining accuracy of a machine tool [9]. It is thus an essential operation for production of precision linear slides used for high-end machine tools and measuring instruments. Before the scraping operation, a measurement operation is carried out to measure the

https://doi.org/10.1515/9783110542363-001

actual flatness of the guideway surface by using an autocollimator [6]. Based on the measured flatness, the excess areas on the guideway surface are roughly scraped away by using a scraper. Then, the autocollimator is used again to identify the residual flatness error of the scraped guideway surface. Such a pair of measurement and scraping operations is repeated until a sub-micrometric flatness is achieved.

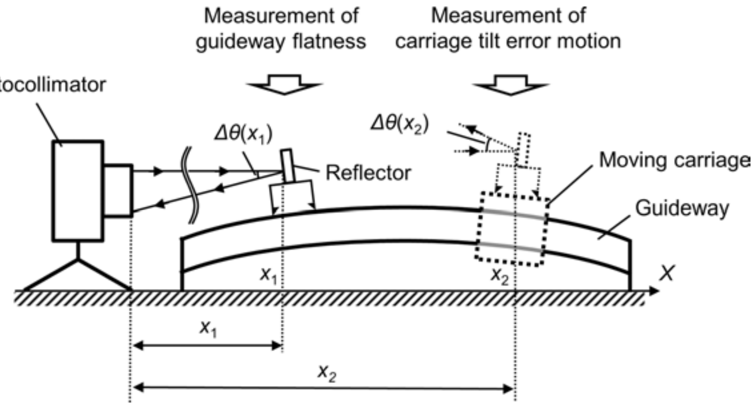

Fig. 1.1: Measurement of slide guideway flatness and carriage title error motion by using an autocollimator.

It is also necessary to link the measured tilt motion error of the moving carriage as well as the measured flatness of the slide guideways with the X-directional positions of the measurement points with a millimeter order accuracy. In the case of the hand scraping operation, the information of the X-direction positions is employed for identifying the positions of the excess areas to be scraped on the guideway surfaces. It has been a problem for a conventional autocollimator since it does have the function for position measurement. It is also a problem for the conventional autocollimator when it is used to measure the tilt motion error of the slide carriage during the assembly process where the linear encoder for closed-loop feedback positioning of the slide table is not available. This makes the error correction process and the assembly process more time-consuming and inefficient. A laser interferometer has a nanometric resolution and a long-range measurement of the displacement of a reflector [10]. A multi-axis laser interferometer with multiple laser beams [11] or a surface encoder based on grating interferometry [12, 13] can also measure the tilt angle of the reflector. However, most of the commercial interferometers are incremental types and can only measure relative displacement instead of absolute position [14]. The output of a laser interferometer will also be lost if the optical path of the laser beam is blocked. The high cost of a laser interferometer is another shortcoming and the high-resolution capability is also not necessary for the millimetric position measurement in the scraping process and the assembly process.

Laser autocollimators, which are composed of a laser light source and an autocollimation unit with a collimator objective (CO) and a light position detector (LPD), have the advantages of fast measurement speed and compact size [15–18]. This chapter presents a laser rangefinder autocollimator, which is a laser autocollimator combining with a low-cost laser rangefinder based on the time-of-flight method [19], for use in the scraping and the assembly processes of a linear slide. A nanoradian laser autocollimator, which can be used for evaluation of an ultrahigh precision linear slide, is also presented [20] together with a PD-edge method associated with laser autocollimation [21, 22].

1.2 Nanoradian laser autocollimator

With the advances in nanotechnology, the resolution of an angle sensor for measurement of an ultraprecision linear slide (linear stage) with a nanometric positioning accuracy is required to be higher than 0.001 arc-second (5 nanoradians). The resolution of a laser interferometer system is typically lower than 0.04 arc-second [23]. An autocollimator employing a CO with a long focal length can achieve a resolution of 0.005 arc-second with a charge-coupled device [24] or 0.002 arc-second with an analog silicon-based sensor [25]. However, such autocollimators tend to be bulky; for example, the total length of the sensor head for the autocollimator with a resolution of 0.002 arc-second is more than 270 mm. It is sometimes difficult to employ such a large autocollimator in the production line of ultraprecision linear stages where the space is restricted. It is thus more desirable to improve the resolution of laser autocollimation [26] that has the advantage of compactness.

As shown in the previous section, a bi-cell photodiode (BPD) or a quadrant photodiode (QPD) is typically employed as a LPD to achieve a high response speed. For such a laser autocollimator, the measurement sensitivity does not depend on the focal length of the CO and a resolution of 0.01 arc-second has been achieved with a short focal length where the focused light spot on the QPD has a small diameter comparable to the QPD cell gap [27]. However, it is difficult to further improve the resolution since most of the energy in the focused light spot with a further smaller diameter will be lost at the insensitive areas (gaps) of QPD, resulting in a degradation of a signal to noise ratio (S/N) of the autocollimator output [28]. As a solution to this problem, a new optical configuration with single-cell photodiodes (SPDs) is presented in this section for angle measurement with a nanoradian-order resolution.

The optical configuration of a two-directional (2D)-type nanoradian laser autocollimator is shown in Fig. 1.2 [18, 20, 22]. A laser diode (LD) and SPDs (SPD1, SPD2 and SPD3) are employed as the light source and LPDs, respectively. The light beam from LD is formed to be a collimated measurement beam by a collimating lens (CL). For simplicity, the divergence of the collimated measurement beam is not considered in the following discussions. After being reflected from the reflector surface, the beam is divided into two parts by using a beam splitter (BS1). One part is made incident to SPD3 for monitoring the intensity fluctuation of LD. The other part is further divided into two sub-beams again by using another beam splitter (BS2). The two sub-beams are made to focus on the SPD1 and SPD2 planes through the COs CO1 and CO2, respectively. The combinations of SPD1/CO1 and SPD2/CO2 are used as the autocollimation units of θ_Y and θ_Z, respectively.

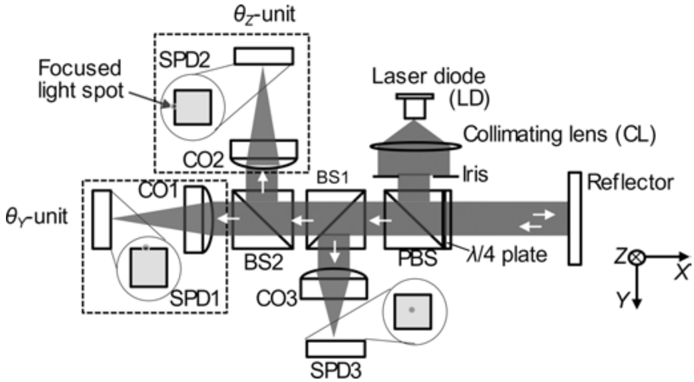

Fig. 1.2: Optical configuration for a 2D-type nanoradian laser autocollimator with single-cell photodiodes (SPDs).

In the θ_Y unit, the focused light spot is positioned on the edge of the PD cell of SPD1 to detect the light spot displacement $\Delta u(v)$ due to the tilt motion $\Delta\theta_Y$. Similar to that shown in eq. (1.1), the relationship between $\Delta\theta_Y$ and $\Delta u(v)$ can be described by the following equation:

$$\Delta u(v) = f \cdot \tan 2\theta_{Y(Z)} \approx 2f\Delta\theta_{Y(Z)} \tag{1.1}$$

where f is the focal length of CO1.

Assume the center of the focused light spot is positioned on the edge of the PD cell on SPD1 when $\Delta\theta_Y = 0$, and the intensity distribution of the light spot on the plane of SPD1 is denoted by $I_1(u,v)$. The output of the θ_Y-unit $u_{\text{SPD\_out}}$ [%] can be calculated by the following equation:

$$u_{\text{SPD\_out}} = \frac{\iint_{S1} I_1(u,v)dudv}{\iint_{S1\_\text{total}} I_1(u,v)dudv} \times 100 \tag{1.2}$$

where S_1 means the area of the light spot received by the PD cell of SPD1. S_{1_total} is the total area of the light spot on the plane of SPD1. The numerator in eq. (1.2) can be estimated from the magnitude of the photocurrent output of SPD1 and the denominator can be estimated from half of the magnitude of the photocurrent output of SPD3.

Similarly, the output of the θ_Z-unit $v_{\text{SPD\_out}}$ [%] can be calculated by

$$v_{\text{SPD\_out}} = \frac{\iint_{S2} I_2(u,v)dudv}{\iint_{S2\_\text{total}} I_2(u,v)dudv} \times 100 \tag{1.3}$$

where $I_2(u,v)$ is the intensity distribution of the light spot on the plane of SPD2. S_2 is the area of the light spot received by the PD cell of SPD2. S_{2_total} is the total area of the light spot on the plane of SPD2. The numerator and denominator in eq. (1.3) can be estimated from the magnitudes of the photocurrent outputs of SPD1 and SPD3, respectively.

If $I_1(u,v)$ and $I_2(u,v)$ are uniform distribution, eqs. (1.2) and (1.3) can be simplified as follows:

$$u_{\text{SPD\_out}} = \frac{\frac{1}{2}\pi(d_1/2)^2 + d_1 \cdot \Delta u}{\pi(d_1/2)^2} \times 100 = 50 + \frac{8f\Delta\theta_Y}{\pi d_1} \times 100 \tag{1.4}$$

$$v_{\text{SPD\_out}} = \frac{\frac{1}{2}\pi(d_2/2)^2 + d_2 \cdot \Delta v}{\pi(d_2/2)^2} \times 100 = 50 + \frac{8f\Delta\theta_Z}{\pi d_2} \times 100 \tag{1.5}$$

where D_{s1} and D_{s2} are the diameters of the focused light spot on the planes of SPD1 and SPD2, respectively. Differing from the case of using QPD, there is no restriction on the acceptable focused light spot diameters D_{s1} and D_{s2} when an SPD is employed for light position measurement. The measurement sensitivity can therefore be maximized by minimizing the focused light spot diameters D_{s1} and D_{s2} to the light diffraction limit. As a result, the optical configuration shown in Fig. 1.2 is expected to achieve a higher measurement resolution compared with that achieved using QPDs.

When the CO is free from aberrations, the focused light spot diameter d_{diff} on the focal plane of the CO will be determined by the diffraction limit as shown in Fig. 1.3. Assume that the light beam of diameter D_0 received by the CO has a uniform intensity distribution. d_{diff} can be expressed by the following equation [29]:

$$d_{\text{diff}} = \frac{2.44f\lambda}{D_0} \tag{1.6}$$

where λ and D_0 are the wavelength and the diameter of the collimated beam from CL, respectively. The focal plane of an aberration-free system is often referred to as a paraxial focal plane [29]. Meanwhile, in practice, the CO is not free from the aberrations. As a result, the focused light spot diameter at the paraxial focal plane will be affected by the aberration. For the laser autocollimator, the spherical aberration is one of the factors dominating the diameter. As can be seen in Fig. 1.4, when D_0 becomes large, a marginal ray strikes the position with a distance of d_{TA} from the optical axis on the paraxial focal plane due to the influence of the spherical aberration. d_{TA} can be determined by the Gaussian optics as follows [30]:

$$d_{TA} = \frac{D_0{}^3}{32f^2(n-1)^2}\left[n^2 - (2n+1)\frac{R_2}{R_2 - R_1} + \frac{n+2}{n}\left(\frac{R_2}{R_2 - R_1}\right)^2\right] \tag{1.7}$$

where n, R_1 and R_2 are the refractive index and surface radii of the CO, respectively. From eq. (1.7), it can be seen that the influence of the spherical aberration increases with the increase of D_0. According to eqs. (1.6) and (1.7), an increase in D_0 will cause a decrease of d_{diff} but an increase of d_{TA}, which has opponent effects on the measurement resolution of light spot position by SPD. Therefore, both the influences of light diffraction and spherical aberration need to be taken into consideration in the determination of D_0 for the nanoradian laser autocollimator. It should be noted that the spherical aberration not only causes an increase in the diameter of the focused light spot, but also causes a disturbance in its intensity distribution, which influences the sensitivity of the laser autocollimator. In the following, computer simulation is carried out based on wave optics to investigate the influences of the spherical aberration.

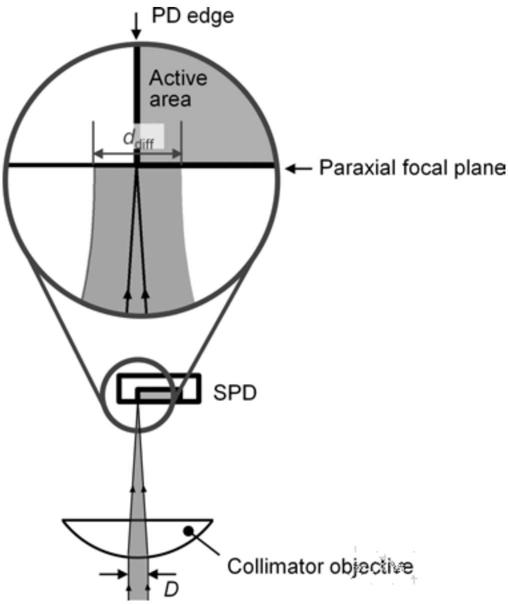

Fig. 1.3: Focused light spot without the influence of spherical aberration.

Figure 1.5 shows an optical model for simulating the autocollimation unit. In the optical model, a plano-convex lens is employed as the CO, while a pupil plane and the SPD plane are placed at its front focal position and back focal position, respectively. The pupil plane having an aperture diameter of D is included in the optical model so that the corresponding measurement beam diameter D_0 can be adjusted. The intensity distribution of the focused light spot $I_1(u,v)$ on the SPD plane can be described by the following equation [31]:

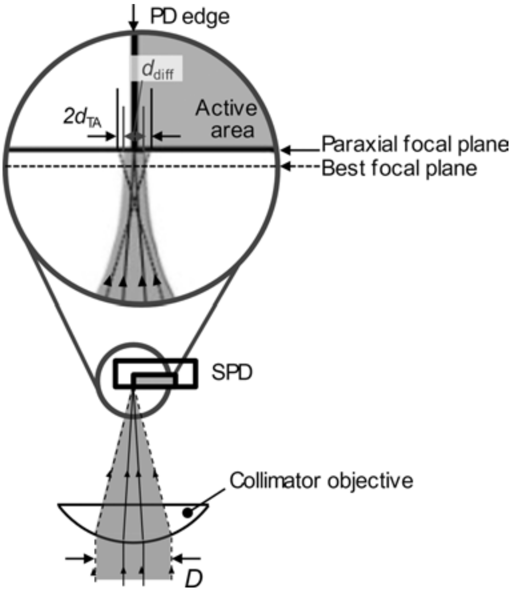

Fig. 1.4: Focused light spot with the influence of spherical aberration.

$$I_1(u,v) = \frac{1}{\lambda^2 f^2}\left|\iint U_l(x,y)P(x+u,y+v)\exp\left[-j\frac{2\pi}{\lambda f}(xu+yv)\right]dxdy\right|^2 \tag{1.8}$$

where $P(x,y)$ and $U_l(x,y)$ are a pupil function and a complex field across the pupil plane, respectively. The pupil function $P(x,y)$ is defined as follows:

$$P(x,y) = \begin{cases} 1 & (\text{when}\, \rho(x,y) < 1) \\ 0 & (\text{when } 1 < \rho(x,y)) \end{cases} \tag{1.9}$$

where $\rho(x,y)$ is the normalized radial coordinate, and can be described as follows:

$$\rho(x,y) = \frac{\sqrt{x^2+y^2}}{D/2} \tag{1.10}$$

Once $I(u,v)$ is calculated from eq. (1.8), the autocollimator outputs can be calculated from eqs. (1.4) and (1.5). In the optical model, the pupil plane is assumed to be illuminated by a plane wave with an amplitude of A uniformly across the surface. The influence of the spherical aberration of the CO can be expressed as a wavefront error, and can be implemented in the calculation by using the complex field $U_l(x,y)$. In the following calculations, $U_l(x,y)$ represented by the following equations is applied to eq. (1.8) [30, 31]:

$$U_l(x,y) = \begin{cases} A \text{ (without aberration)} \\ A \cdot \exp\left[j\frac{2\pi}{\lambda}S\rho^4(x,y)\right] \text{ (with aberration, at paraxial focus)} \\ A \cdot \exp\left[j\frac{2\pi}{\lambda}S(\rho^4(x,y)-\rho^2(x,y))\right] \text{ (with aberration, at best focus)} \end{cases} \tag{1.11}$$

where S is referred to as the peak aberration coefficient. In the case of a plano-convex lens, S can be described by [30, 32]

$$S = \frac{-\left[n^3+(n+2)+(3n+2)\,(n-1)^2-4(n^2-1)\right]\cdot D^4}{32n(n-1)^2 f^3} \tag{1.12}$$

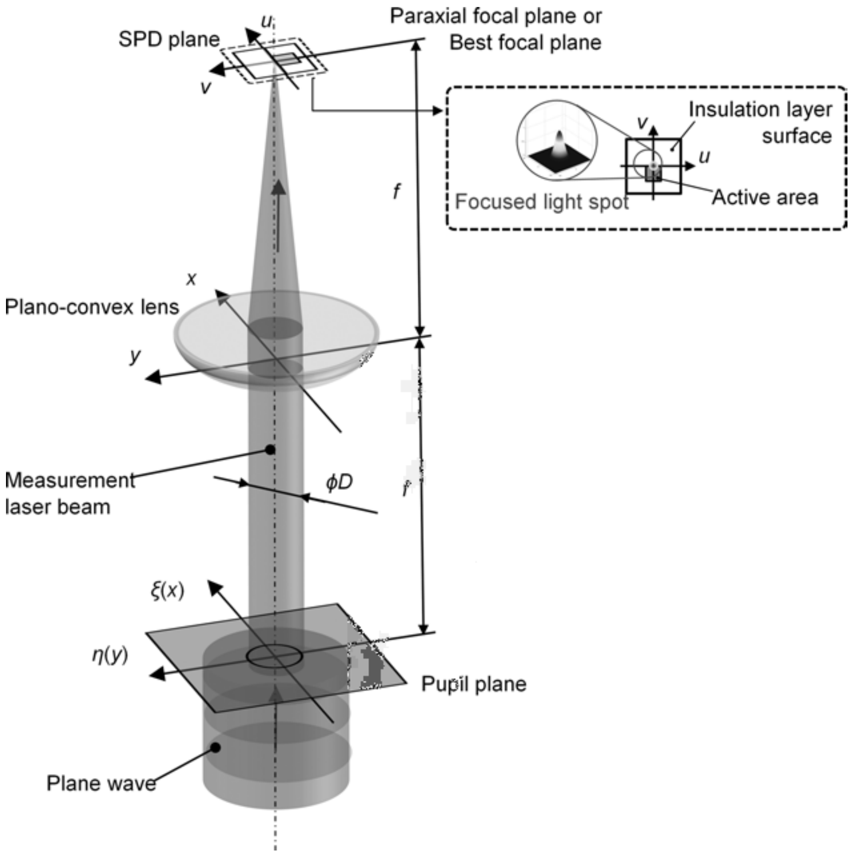

Fig. 1.5: An optical configuration for computer simulation based on wave optics.

Parameters employed in the following calculations are summarized in Tab. 1.1. The values of the parameters are determined to be consistent with the following experiments. Figures 1.6, 1.7 and 1.8 show examples of the $U_l(x,y)$ calculated by using the parameters in Tab. 1.1. The wavefront errors are represented in a wave number. As shown in Fig. 1.7, the influence of the spherical aberration becomes significant near the edge of the projected aperture diameter.

Tab. 1.1: Parameters used in the computer simulation.

Parameter	Value	Unit
Wavelength (λ)	685	[nm]
Focal length of the collimator objective (f)	100	[mm]
Refractive index of the collimator objective (n)	1.517	–
Aperture diameter on the pupil plane (corresponding to the measurement laser beam diameter) (D)	1–14	[mm]

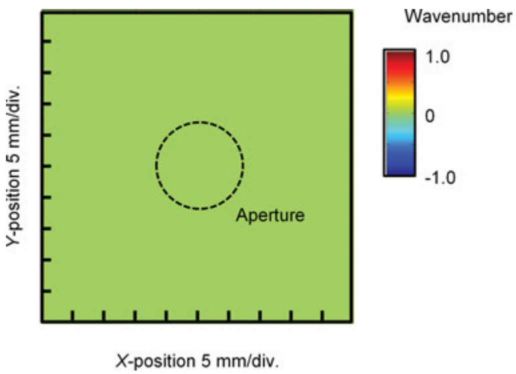

Fig. 1.6: Wavefront errors due to the spherical aberration of the collimator objective applied to the simulation model (D_0 = 14 mm) without the spherical aberration.

At first, the relationship between the intensity distribution $I_1(u,v)$ and the beam diameter D_0 is calculated. Figures 1.9 and 1.10 show the calculated $I_1(u,v)$ for D_0 of 2 and 14 mm, respectively. The cross sections of the results are shown in Figs. 1.11 and 1.12, respectively. In the figures, $I_1(u,v)$ is normalized by the maximum intensity calculated with the aberration-free system In the case of small D_0 (=2 mm) shown in Fig. 1.9, the influence of the spherical aberration on $I_1(u,v)$ at the paraxial focal plane is negligibly small. However, the influence becomes large with the increase of D_0, as shown in Fig. 1.10. Meanwhile, even under the influence of the spherical aberration, $I_1(u,v)$ at the best focal plane is found to be almost identical to that calculated with the aberration-free system.

The $1/e^2$ diameter of the focused light spot on the SPD plane is then calculated with respect to D_0 based on the results of Figs. 1.11 and 1.12. As shown in Fig. 1.13, the $1/e^2$ diameter of the focused light spot at the best focus continuously decreases

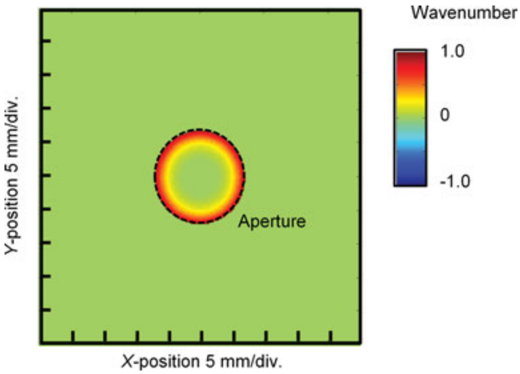

Fig. 1.7: Wavefront errors due to the spherical aberration of the collimator objective applied to the simulation model (D_O = 14 mm) without the spherical aberration with the spherical aberration, at paraxial focal plane.

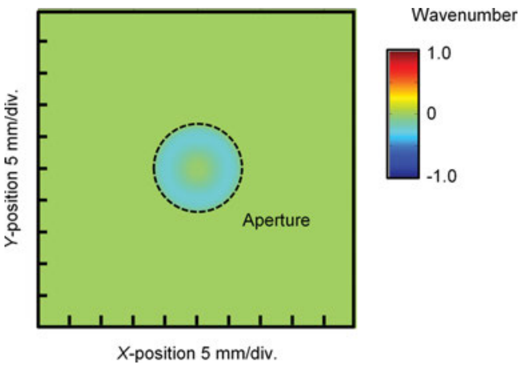

Fig. 1.8: Wavefront errors due to the spherical aberration of the collimator objective applied to the simulation model (D_O = 14 mm) without the spherical aberration with the spherical aberration, at the best focal plane.

with the increase of D_O. On the other hand, the diameter at the paraxial focus decreases and increases with the increase of D_O when D_O is smaller and larger than 11 mm, respectively.

By using the results of Fig. 1.9, the output u_{SPD_out} of laser autocollimator is calculated. Figure 1.14 shows the calculation procedure. At first, the total power of the focused light spot on the whole SPD plane is calculated. After that, the relationship between the displacement of the focused light spot Δu_i and the tilt angle $\Delta\theta_{Yi}$ of the reflector is evaluated. The sum of the total power of the focused light spot on the SPD active area is then calculated. Finally, u_{SPD_out} at each $\Delta\theta_{Yi}$ is evaluated.

Figures 1.15 and 1.16 show the results of simulation for D_O of 2 mm and 14 mm, respectively. The curves of the autocollimator output u_{SPD_out} versus the tilt motion

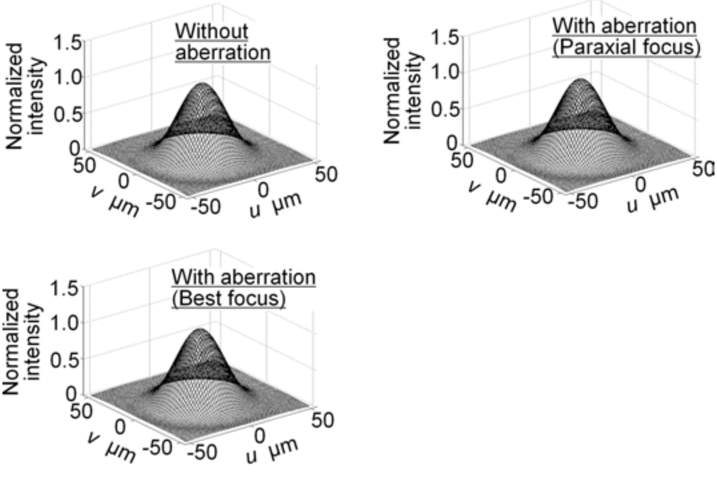

Fig. 1.9: Calculated intensity distribution of the focused light spot on the SPD plane. $D = 2$ mm.

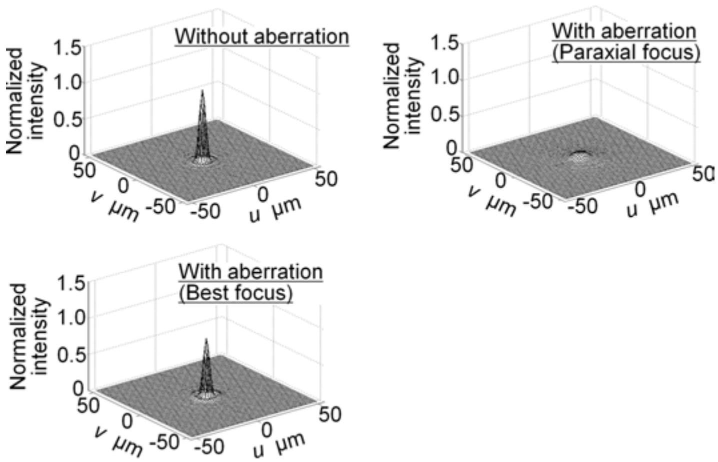

Fig. 1.10: Calculated intensity distribution of the focused light spot on the SPD plane. $D = 14$ mm.

of the reflector $\Delta\theta$($u_{\text{SPD\_out}}$–$\Delta\theta$ curves) are plotted in the figures. The sensitivities of the autocollimator outputs are also calculated from the data in the $u_{\text{SPD\_out}}$–$\Delta\theta$ curves for $\Delta\theta$ of –5 arc-seconds to 5 arc-seconds. The results are plotted in Fig. 1.17. As shown in Fig. 1.15, the $u_{\text{SPD\_out}}$–$\Delta\theta$ curves are almost the same regardless of the existence of the spherical aberration when D_0 is 2 mm. When D_0 is 14 mm, however, the sensitivity of the autocollimator decreases significantly at the paraxial focal plane as shown in Fig. 1.16. It should be noted that the sensitivity clearly decreases

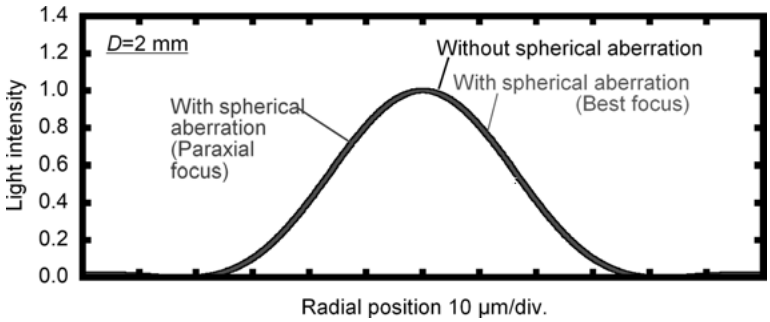

Fig. 1.11: Cross sections of the intensity distributions in Fig. 1.9.

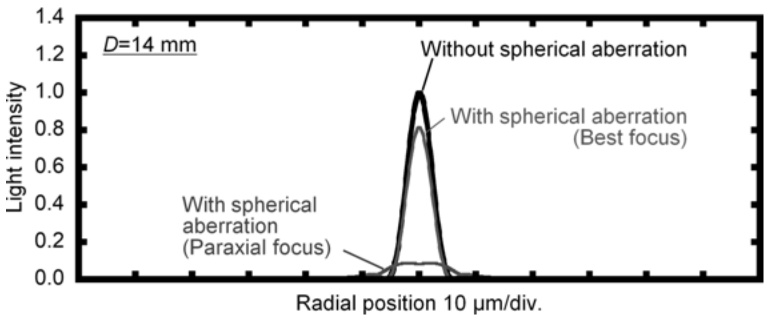

Fig. 1.12: Cross sections of the intensity distributions in Fig. 1.10.

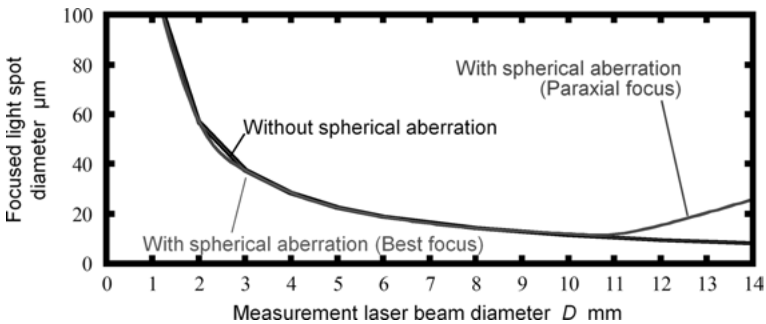

Fig. 1.13: Variation of the focused light spot diameter on the SPD plane.

at the best focal plane under the influence of the spherical aberration, even though the laser beam diameter is almost the same as that of the aberration-free system, as shown in Fig. 1.17. From these results, it is revealed that a slight disturbance in the intensity distribution can cause a decrease in the sensitivity of the autocollimator output.

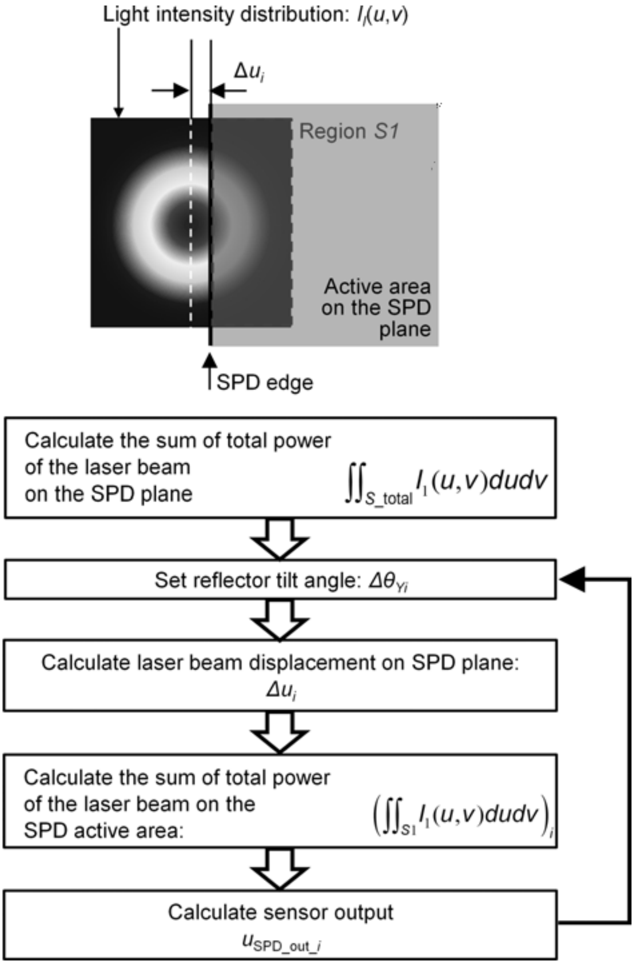

Fig. 1.14: Calculation procedure for calculation of the laser autocollimator output.

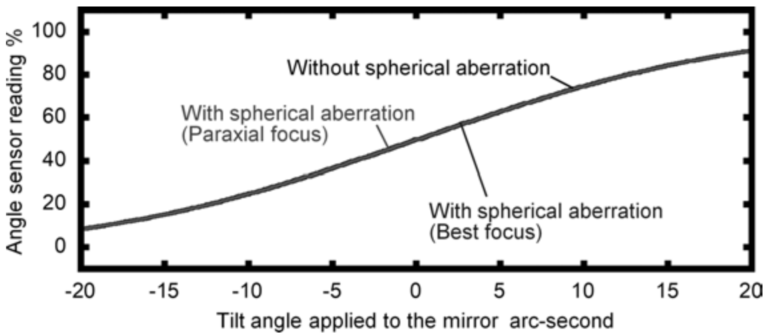

Fig. 1.15: Calculated u_{SPD_out}–$\Delta\theta$ curves. $D = 2$ mm.

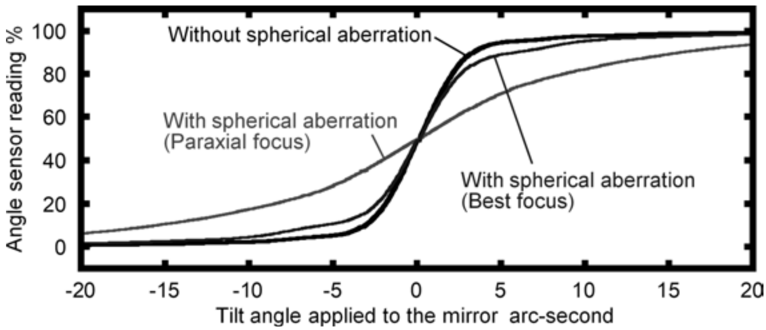

Fig. 1.16: Calculated $u_{\mathrm{SPD\_out}}$–$\Delta\theta$ curves. $D = 14$ mm.

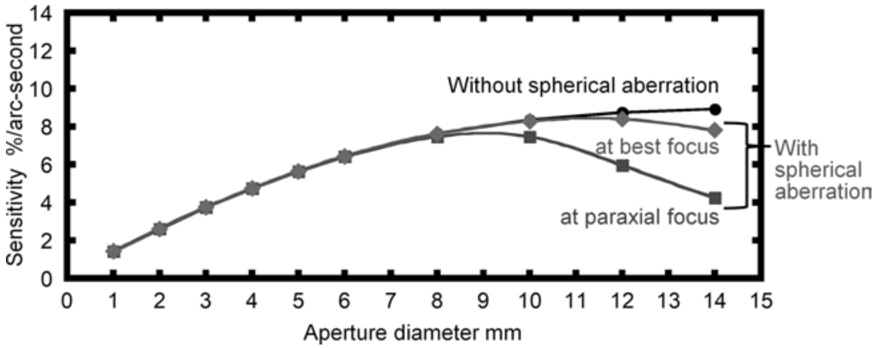

Fig. 1.17: Variation of sensitivity as a function of D_0.

The results of the computer simulation were compared with those of experiments. At first, the influence of the spherical aberration on the focused light spot diameter was investigated experimentally. Figure 1.18 shows a schematic of the experimental setup. A laser beam from a 685 nm wavelength LD was collimated by using an aspherical lens. The collimated laser beam was then expanded by using a beam expander, and the expanded laser beam was made to pass through a diameter-variable iris. The beam expander was employed not only for expanding the laser beam diameter but also for making the intensity distribution of the laser beam to passing through the iris as uniform as possible. The laser beam that had passed through the iris with an aperture diameter of D_0 was then made to go through a plano-convex CO with a focal length f of 100 mm. The focused light spot was monitored by a commercial beam profiler (BeamScan XYS/LL/5 µm, Photon Inc.). At the beginning of the experiment, the position of the beam profiler along the optical axis was adjusted with a narrow laser beam with a diameter D_0 of 2 mm. The beam profiler was kept stationary during the experiment at a position almost identical to the paraxial focus. The variation of the $1/e^2$ diameter of the focused light spot was measured

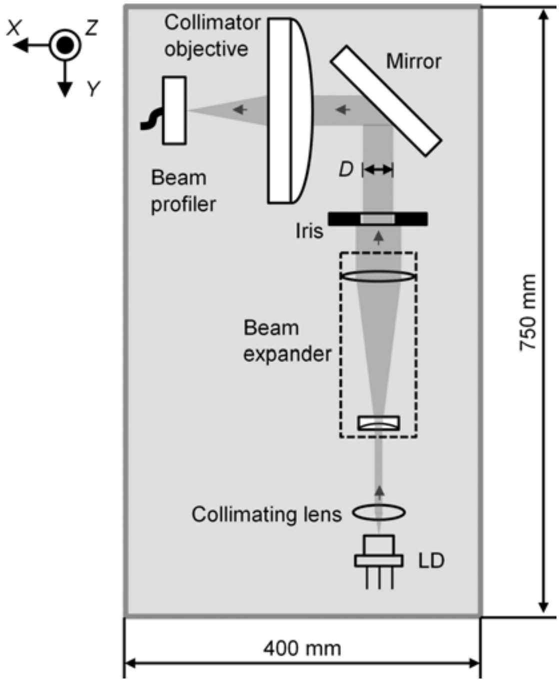

Fig. 1.18: Experimental setup for measurement of the focused light spot.

when D_0 was increased from 2 to 14 mm, Fig. 1.19 shows the results. In the figure, the focused light spot diameter calculated in the simulation is also plotted. A good agreement can be found between the results of the simulation and the experiment.

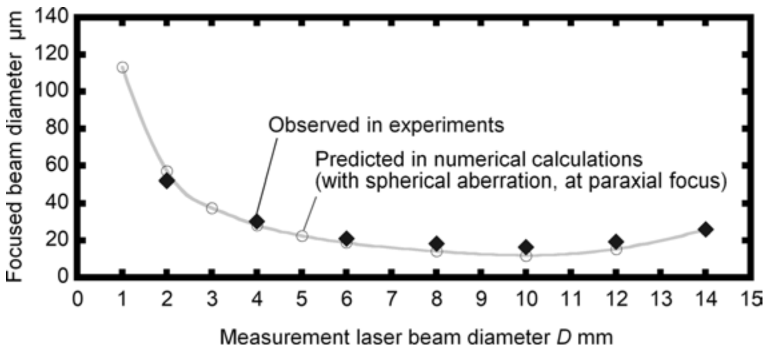

Fig. 1.19: Measured focused light spot diameter.

A laser autocollimation unit was constructed for investigating the influence of the spherical aberration on the sensitivity of the autocollimation unit output. Figure 1.20 shows the optical configuration of the autocollimator unit. The reflector in Fig. 1.18 was mounted on a piezoelectric (PZT) tilt stage, which had been calibrated by using a commercial autocollimator (Möller–Wedel Optical GmbH, Elcomat 3,000). The beam profiler in Fig. 1.18 was replaced with the autocollimation unit, which consists of a BS and two SPDs: SPD1 and SPD2. Both SPD1 and SPD2 were placed on the focal plane of the CO. SPD1 was aligned on the focal plane in such a way that the center of the focused light spot was made to coincide with the edge of the PD cell. Meanwhile, the PD cell of SPD2 was aligned to capture the whole energy of the focused light spot. It should be noted that the alignments of the SPDs were carried out by setting the iris aperture diameter D_0 to be 2 mm. The PD cell of SPD1 was located at a position almost identical to the paraxial focus. Bi-cell Si PIN photodiodes (Hamamatsu S4204) were employed for the SPDs. As shown in Fig. 1.21, one of the PD cells of the photodiode was employed as the SPD1.

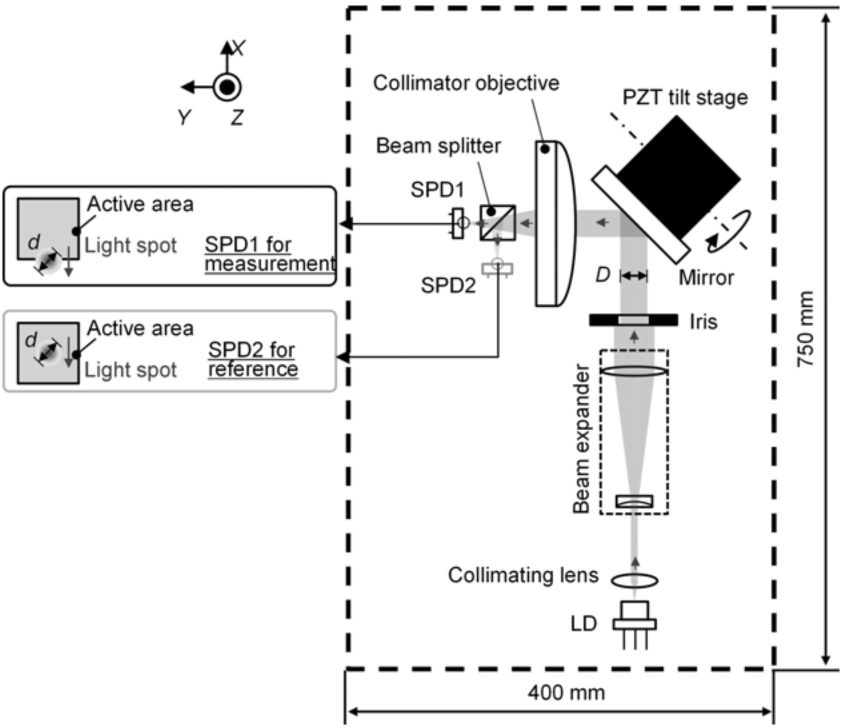

Fig. 1.20: A schematic of the laser autocollimation unit for evaluation experiment of sensitivity.

In the experiments, a continuous sinusoidal tilt motion was applied to the reflector via the PZT tilt stage. Photocurrent outputs from SPD1 and SPD2 were converted into voltage outputs by transimpedance amplifiers. The voltage outputs were recorded simultaneously by a digital oscilloscope. Figures 1.22, 1.23 and 1.24 show the

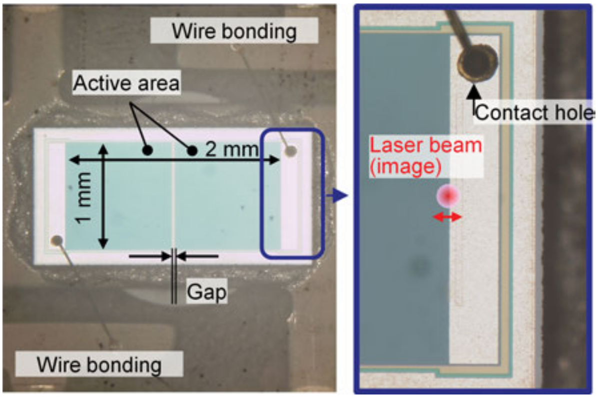

Fig. 1.21: Pictures of the SPD1.

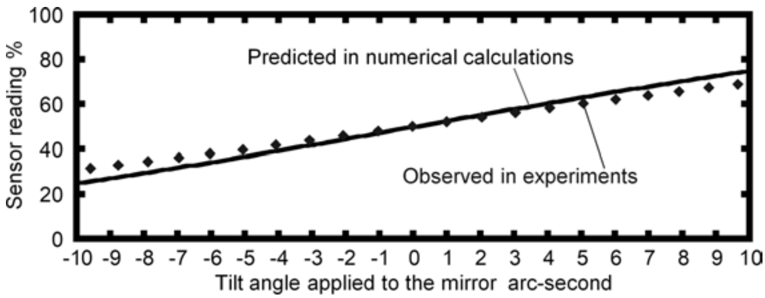

Fig. 1.22: Measured $u_{\text{SPD\_out}}$–$\Delta\theta$ curves. $D_0 = 2$ mm.

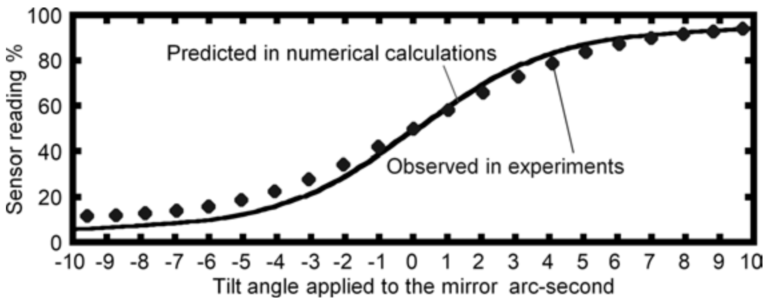

Fig. 1.23: Measured $u_{\text{SPD\_out}}$–$\Delta\theta$ curves. $D_0 = 10$ mm.

measurement results for different D_0. In the figure, the calculated $u_{\text{SPD\_out}}$–$\Delta\theta$ curves by simulation are also plotted. The sensitivities of the autocollimation unit outputs, which were calculated from the data in the measured $u_{\text{SPD\_out}}$–$\Delta\theta$ curves ranging from $\Delta\theta$ of –5 to 5 arc-seconds, are shown in Fig. 1.25. As can be seen in the figure, it is effective to improve the sensitivity by increasing D_0 when D_0 was smaller than 10 mm. On the other hand, the sensitivity decreased with the increase of D_0 when D_0 was larger than 10 mm, which was due to the influence of spherical aberration of the CO. The results of the experiments were consistent with those of simulation.

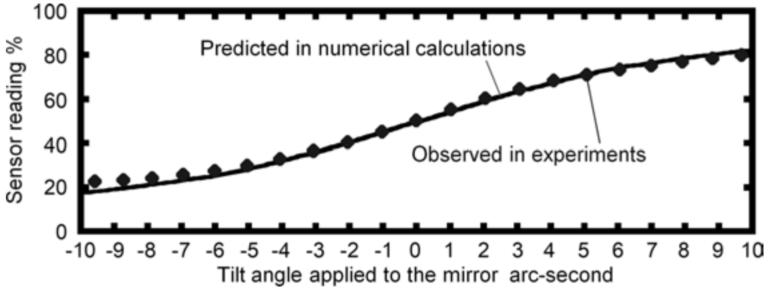

Fig. 1.24: Measured u_{SPD_out}–$\Delta\theta$ curves. D_0 = 14 mm.

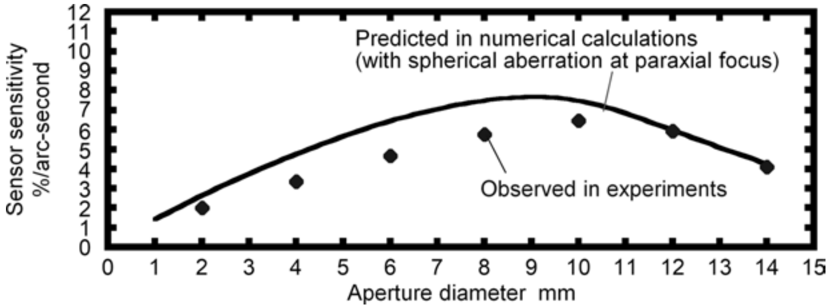

Fig. 1.25: Comparison of sensitivities by experiments and simulation.

A nanoradian laser autocollimator with a compact size was then designed and constructed based on the results of simulation and experiments shown above. Figure 1.26 shows the optical layout of the nanoradian laser autocollimator. It is a one-directional (1D) type that is simplified from the 2D type shown in Fig. 1.20. The autocollimator was designed in a size of 100 mm (X) × 150 mm (Y). The same LD with a wavelength of 685 nm in Figs. 1.18 and 1.20 was employed as the light source. The transimpedance amplifier and the digital oscilloscope in Figs. 1.18 and 1.20 were also employed. However, the beam expander in Figs. 1.18 and 1.20 was not employed due to the limitation in sensor size. A CL, which was provided by an optics manufacturing company, was selected for generating a measurement laser beam that had a smooth intensity distribution profile with reduced interference and speckle noises. The diameter of the measurement laser beam was 5 mm, which was determined by the CL. For this reason, investigation of the effect of a beam diameter D_0 on the angular resolution was limited within 5 mm in the following experiment. An optical isolator, which was a combination of a polarizing beam splitter (PBS) and a quarter-wave plate was employed to avoid the influence of stray light rays on the laser source. An achromatic doublet lens with reduced spherical aberration was employed as the CO. The focal length of the CO was set to be 100 mm. The same photodiodes shown in Fig. 1.21 were utilized as the SPDs. A picture of the nanoradian laser autocollimator is shown in Fig. 1.27, which was built on a vibration isolation table. A flat mirror reflector was mounted on the PZT tilt stage.

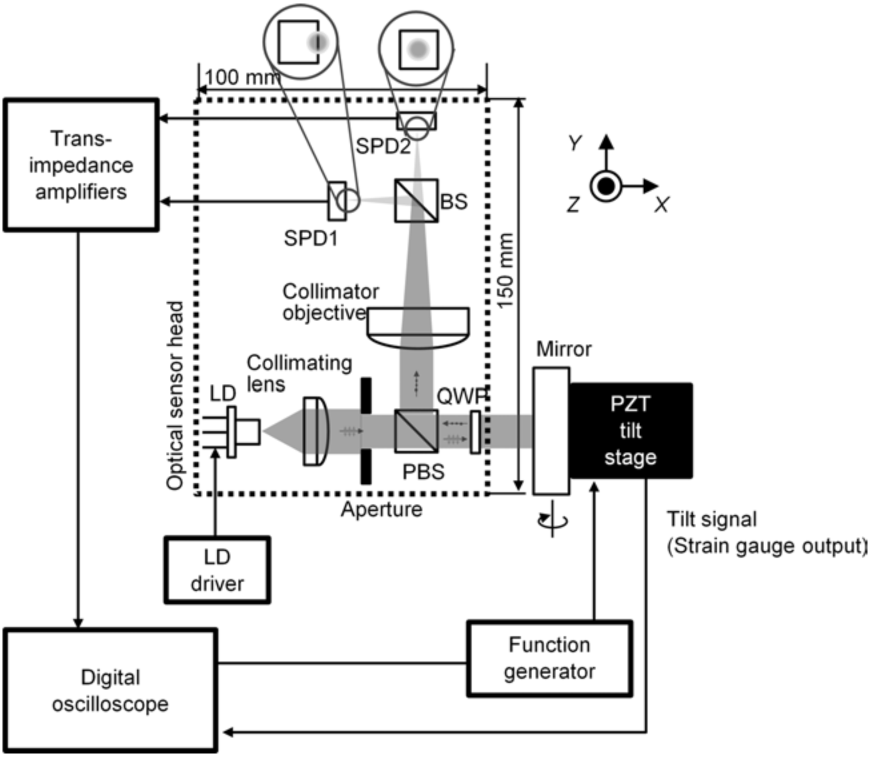

Fig. 1.26: Optical layout of the nanoradian laser autocollimator.

The short-term stability of the nanoradian laser autocollimator was tested, from which the angular resolution could be estimated. The center of the focused light spot was aligned to be on the edge of the PD cell of SPD1 by using the PZT tilt stage for the test. During the test, the tilt stage was kept stationary and the outputs from SPD1 and SPD2 were captured. The variation of the voltage outputs of SPD1 over a term of 5 s is shown in Fig. 1.28. The standard deviation (σ) of the voltage outputs from both the SPD1 and SPD2 was confirmed to be approximately 0.3 mV, corresponding to a fluctuation of the sensor output of approximately 0.00323%.

The $u_{\mathrm{SPD\_out}}$–$\Delta\theta$ curves were measured by applying a periodic sinusoidal tilt motion about the Y-axis was applied to the reflector, from which the sensitivity of the

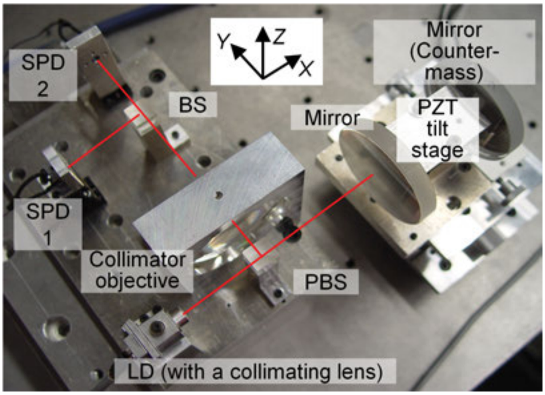

Fig. 1.27: Picture of the nanoradian laser autocollimator.

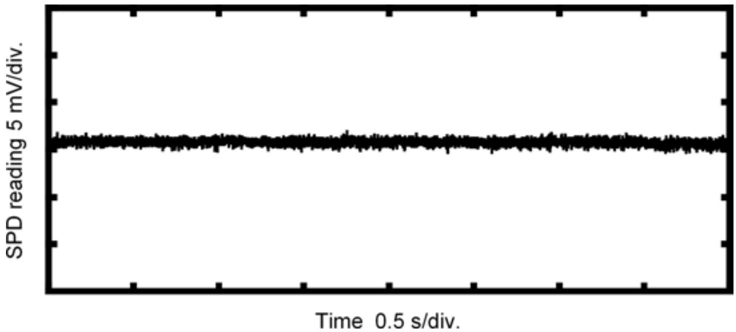

Fig. 1.28: A typical waveform of the SPD output through the transimpedance amplifier.

nanoradian laser autocollimator output could be evaluated. Figure 1.29 shows the measured $u_{\mathrm{SPD\_out}}$–$\Delta\theta$ curves. In the measurement, D_0 was adjusted by inserting an aperture between the CL and the PBS as shown in Fig. 1.26. The results by simulation are also shown in Fig. 1.29 for comparison. The sensitivities of the nanoradian laser autocollimator outputs were calculated by using the data in the measured $u_{\mathrm{SPD\_out}}$–$\Delta\theta$ curves ranging from $\Delta\theta$ of −5 to 5 arc-seconds. As expected, the sensitivity was improved in proportion to D_0. A fairly good correlation can be found between the results of the computer simulation and experiments. When D_0 was set to be 5 mm, the sensitivity was 4.57%/arc-second. Regarding the fluctuation of the output shown in Fig. 1.30 (0.00323%), a resolution of approximately 0.0007 arc-second (3.4 nrad) is expected to be achieved by the nanoradian laser autocollimator.

Dynamic tilt motion measurements were carried out by using the nanoradian laser autocollimator. The outputs of the laser autocollimator were acquired when a periodic sinusoidal tilt motion with an amplitude and a frequency of 0.001 arc-second (4.8 nrad) and 1 Hz, respectively was applied to the reflector by the PZT tilt stage. The results are shown in Fig. 1.31. In the experiment, D_0 was set to be 5 mm. It

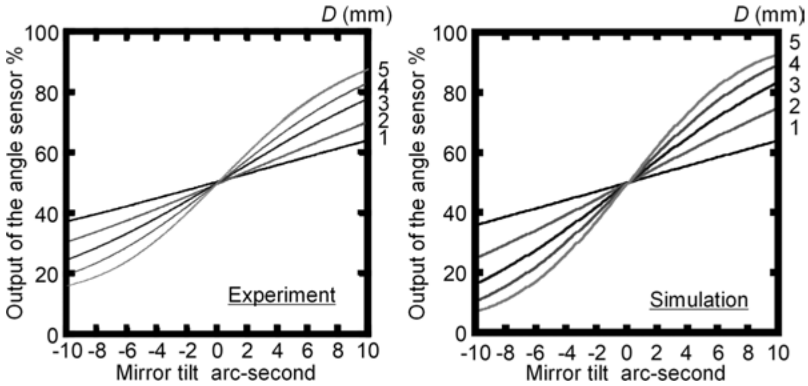

Fig. 1.29: The u_{SPD_out}–$\Delta\theta$ curves of the nanoradian laser autocollimator by experiment and simulation.

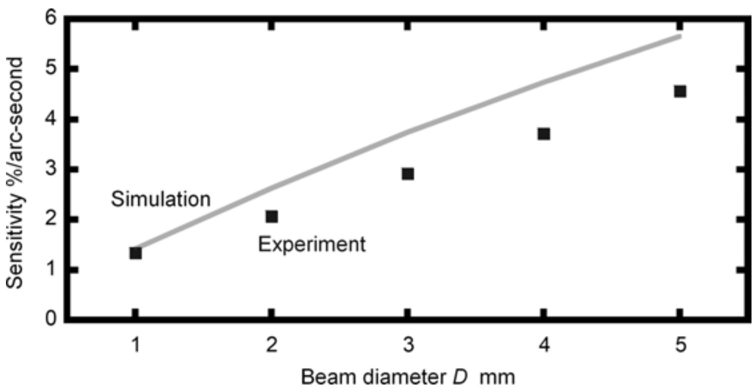

Fig. 1.30: Sensitivities of the nanoradian laser autocollimator.

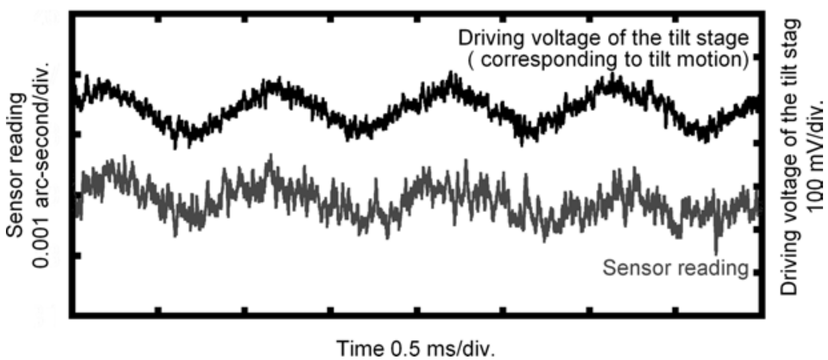

Fig. 1.31: Measurement result of a nanoradian angular motion.

can be seen in the figure that the sinusoidal tilt motion was clearly detected, verifying the capability of the laser autocollimator for nanoradian angle measurement.

1.3 Rangefinder autocollimator

As shown in Fig. 1.1, an autocollimator is an optical instrument used with a reflector for measurement of the tilt angle of the reflector. The autocollimator has the advantages of easy use, high measurement resolution and long working range [27]. During the hand scraping process as well as the assembly process, the optical path of the autocollimator may be intermittently blocked by the operator. The measurement can be re-started from the blocked position without losing the tilt angle information measured by the autocollimator. This is an important feature for practical use in the hand scraping and assembly processes. When the autocollimator is employed for surface flatness measurement in the hand scraping process, the reflecting mirror is fixed on a two-footed base. The base is moved on the surface of the guideway along the X-axis step by step over the length of the surface to be measured in such a way that the forward foot of the base is positioned at the point where the rear foot previously rested. At each of the measurement points, multiplying the reading of the autocollimator and the distance between the two feet of the base gives the height difference between the two feet. The flatness of the guideway surface can thus be obtained from the height difference data [33]. Assuming that the distance between the two feet of the base is 100 mm, a 0.2 arc-second reading of the autocollimator corresponds to a height difference of approximately 0.1 μm, which is good enough for the sub-micrometer flatness measurement of the guideway surface.

In the assembly process, the autocollimator is employed to measure the tilt motion errors (pitch and yaw) of the slide carriage when it is mounted on the guideways. A tilt motion error of the slide carriage is one of the sources for the positioning error of the slide. A linear slide is used to move a cutting tool in a machine tool or a measuring probe in a measuring instrument. In most cases, the cutting position or the measuring position has a certain distance from the slide axis of motion, which is called the Abbe offset. Even a small tilt motion error can generate a sub-micrometric error in the cutting or measuring position (positioning error), which is referred to as the Abbe error [17, 34]. For example, a 0.2 arc-second tilt motion error will cause a positioning error of approximately 0.1 μm for a 100 mm Abbe offset. If the measured tilt motion error is too large, it is necessary to return to the hand scraping process for further correction of the flatness errors of the slide guideways.

Figure 1.32 shows a schematic of a laser rangefinder-autocollimator that can measure both the tilt angle and the position of a reflector by combining an autocollimation unit and a rangefinder unit [19, 35]. The measurement resolutions/ranges for tilt angle and position are set to be 0.2/±40 arc-seconds, 1 mm/5 m, respectively. In the sensor, a LD is employed as the light source. The laser light with a wavelength λ from

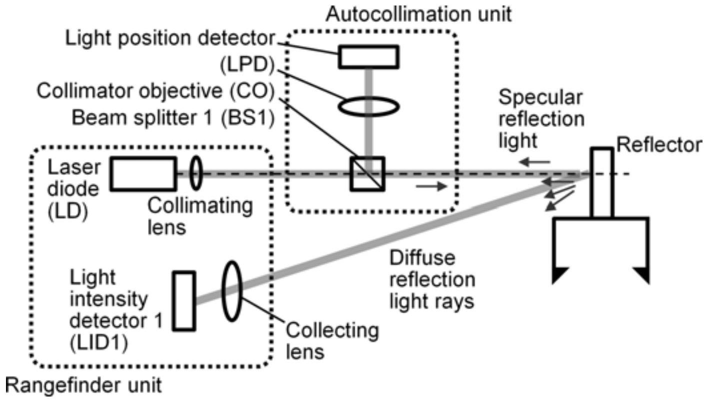

Fig. 1.32: A schematic of the laser rangefinder-autocollimator.

the LD is collimated by using a CL before it is projected onto the target reflector. Denoting the diameter of the output beam at the CL by D_0 and the beam divergence angle by β_{beam}, the beam diameter D_{beam} at a position x can be written by

$$D_{\mathrm{beam}}(x) = D_0 + \beta_{\mathrm{beam}} \cdot x \tag{1.13}$$

It should be noted that the beam divergence is not shown in the figure for the sake of clarity. As shown in the figure, the specular reflection light from the reflector is bent by the BS1 before it enters the autocollimation unit. The autocollimation unit consists of a CO and a LPD placed at the focal position of the objective. Denote the tilt angle of the reflector at position x by $\Delta\theta(x)$, the focal length of the objective by f and the displacement of the focused light spot on the detector by $\Delta d_{\mathrm{LPD}}(x)$, respectively. For a small $\Delta\theta(x)$, it can be expressed by the following equation [36]:

$$\Delta\theta(x) = \arctan\frac{\Delta d_{\mathrm{LPD}}(x)}{2f} \approx \frac{\Delta d_{\mathrm{LPD}}(x)}{2f} \tag{1.14}$$

Meanwhile, in the rangefinder unit for position measurement of the reflector, a collecting lens (CL) is employed to collect a part of the diffuse reflection light rays. If the distance of the reflector from the LD is long enough, the optical path from the LD to the reflector and that from the reflector to the light intensity detector 1 (LID 1) of the rangefinder unit can be regarded as the same. Under this condition, the position x of the reflector can be obtained based on the principle of time of flight from the following equation [37]:

$$x = \frac{c}{2}\Delta t \tag{1.15}$$

where c is the speed of light and Δt is the time for a pulsed light to travel from the LD to the detector via the reflector.

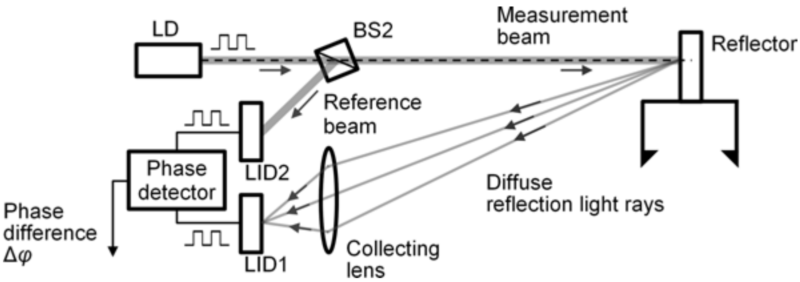

Fig. 1.33: A schematic of the laser rangefinder unit with phase modulation.

As can be seen in eq. (1.15), the resolution of the simple time-of-flight principle is determined by time measurement. For a millimeter position measurement resolution, a pico-second order time measurement resolution is required, which is difficult to achieve. A phase modulation technique [38] shown in Fig. 1.33 is typically employed to improve the resolution of the rangefinder for position measurement. BS2 is added to the optical path of the rangefinder to generate a reference beam. The reference beam is received by LID 2. Assume that the light intensity of the pulsed laser light from the LD is modulated with a frequency f_{ref}. By measuring the phase difference $\Delta\phi$ between the pulse train in the reference laser beam and that in the measurement laser beam, the position x of the reflector can be obtained from the following equation [38]:

$$x = \frac{c}{4\pi f_{\mathrm{ref}}}\Delta\varphi \tag{1.16}$$

Table 1.2 shows the specifications of a commercial laser rangefinder unit that is selected for the laser rangefinder-autocollimator [39]. As can be seen in the table, a modulation frequency of 66.67 MHz is adopted for a position measurement resolution of 1 mm over a range of 30 m [39]. A low price is also an advantage of the laser rangefinder. An autocollimation unit is then designed for integration with the rangefinder unit. At first, the diameter D_C of the CO and the width w_{BS} of BS1 are determined based on Fig. 1.34. It can be seen in the figure that the specular reflection light from the reflector is received by the collimator lens at position P when the tilt angle of the reflector at the position of L_R reaches its maximum ($\Delta\theta_R$). The distance from P to the center O of the CO is denoted by t_R and the laser beam diameter at the CO is denoted by D_{beam} $(2L_R)$. The following equations can be obtained:

$$D_C = 2t_R + D_{\mathrm{beam}}(2L_R) \tag{1.17}$$

Tab. 1.2: Specifications of the commercial laser rangefinder [39].

Item	Value	Unit
Wavelength of laser diode	0.68	[μm]
Resolution	1	[mm]
Range	30	[m]
Modulation frequency (f_{ref})	66.67	[MHz]
Measurement time	0.16	[s]
Beam diameter (D_0)	3	[mm]
Beam divergence angle (b_{beam})	0.16	[rad]
Working temperature	−10–50	[ºC]
Size	172 × 73 × 45	[mm]

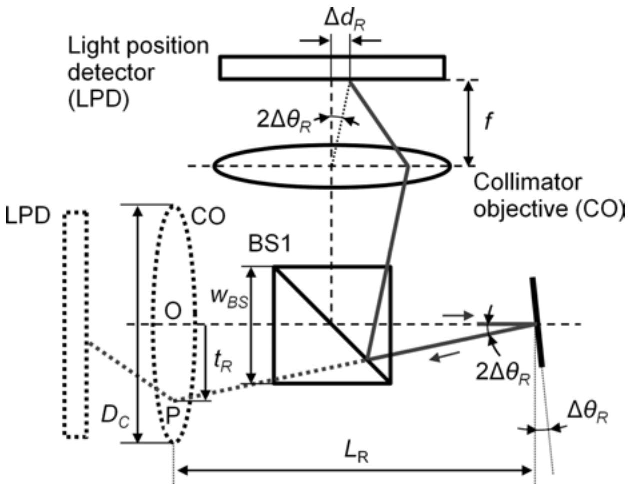

Fig. 1.34: Determination of the diameter of CO and the size of BS1 for the autocollimation unit.

$$t_R = L_R \tan(2\Delta\theta_R) \approx 2L_R\Delta\theta_R \tag{1.18}$$

Substituting eqs. (1.13) and (1.18) in eq. (1.17) gives

$$D_C = D_0 + 2L_R\left(2\Delta\theta_R + \beta_{\text{beam}}\right) \tag{1.19}$$

Based on D_0 (=3 mm), L_R (=5 m), $\Delta\theta_R$ (=40 arc-seconds) and β_{beam} (=0.16 mrad), D_C is calculated to be 8.48 mm. A CO with a diameter of 10 mm was selected based on the result. Similarly, the width of W_{BS} of BS1 is determined to be 10 mm based on the calculated D_C.

A BPD or a QPD can be chosen as the LPD for 1D or 2D angle measurement [16, 26, 40]. Figure 1.35 shows the light spot that is focused on the LPD with a gap of g_{LPD} (=10 µm) by the CO. The diameter D_s of the light spot is expressed by

$$D_S = \frac{4f\lambda}{\pi D_0} + f\beta_{\mathrm{beam}} \tag{1.20}$$

The first term in the right side of eq. (1.20) is determined by light diffraction and the second term is caused by the beam divergence [29].

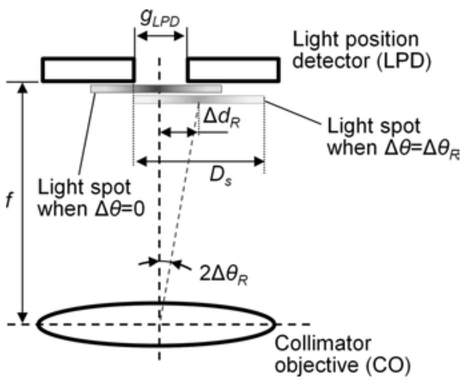

Fig. 1.35: Determination of the focal length of CO for the autocollimation unit.

Assume that the light spot is located at the center of the LPD when the tilt angle of the reflector is zero and the width of the LPD cell is much larger than the diameter of the light spot. The light spot moves a distance of Δd_R to its leftmost or rightmost positions when the tilt angle of the reflector reaches its maximum value of $\Delta\theta_R$. The relationship between g_{LPD}, D_s and Δd_R can be expressed by

$$D_S \geq g_{\mathrm{LPD}} + 2\Delta d_R = g_{\mathrm{LPD}} + 4f\Delta\theta_R \tag{1.21}$$

The focal length of the CO can then be obtained as follows by combining eqs. (1.20) and (1.21):

$$f \geq \frac{g_{\mathrm{LPD}}}{\frac{4\lambda}{\pi D_0} + \frac{\beta_{\mathrm{beam}}}{4} - 4\Delta\theta_R} \tag{1.22}$$

f is calculated to be larger than 63 mm from eq. (1.22) and a CL with a focal length of 80 mm is selected for assurance of a large enough measurement range of tilt angle.

Figure 1.36 shows the layout of the laser rangefinder-autocollimator [19]. A QPD is employed as the light position photodetector in the autocollimation unit for measurement of 2D tilt angles (pitch $\Delta\theta_Y$ and yaw $\Delta\theta_Z$). As can be seen in the figures, the autocollimation unit is placed on the same side as the CL of the rangefinder unit for a compact structure. The size of the laser rangefinder-autocollimator is

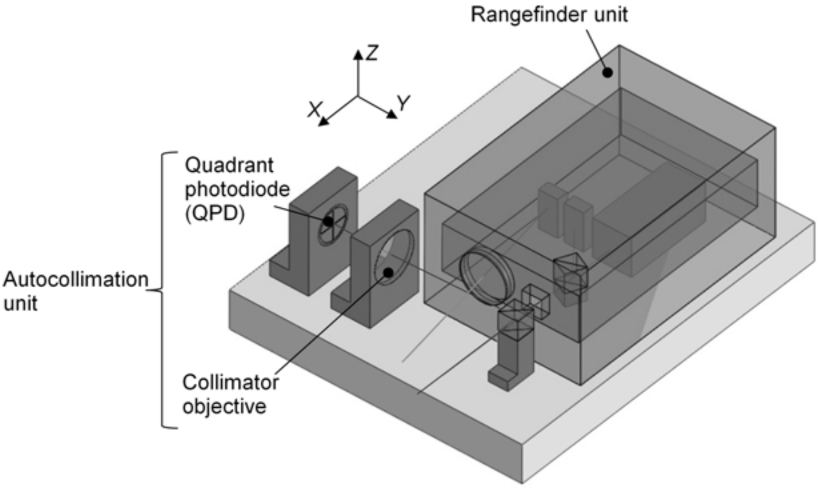

Fig. 1.36: Layout of the laser rangefinder-autocollimator.

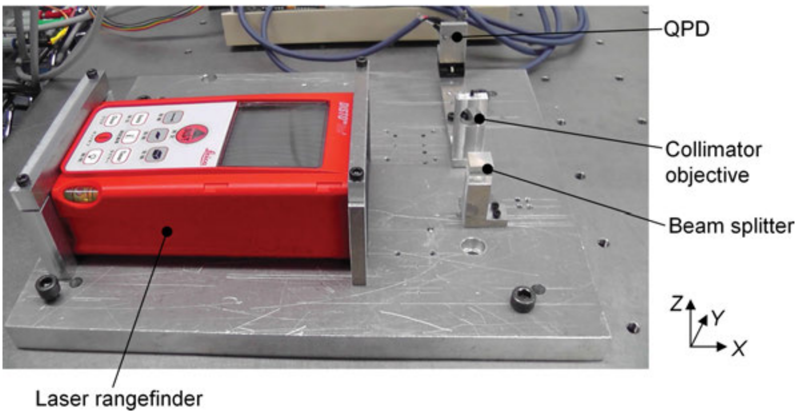

Fig. 1.37: Picture of the laser rangefinder-autocollimator.

250 mm × 205 mm × 63 mm. It is compact enough for use as a standalone measuring instrument in the hand scraping and assembly processes of a precision linear slide. Figure 1.37 shows a picture of the laser rangefinder-autocollimator.

The laser beam from the rangefinder unit works is a high-frequency modulated pulsed laser beam. However, constant laser power is required for the laser autocollimation unit. It is necessary to avoid the influence of the pulsed laser power on the measurement of the autocollimation unit. A sequence shown in Fig. 1.38 is then employed to control the laser power. In each measurement cycle, the laser power is first controlled to be constant in the term T_1 for the measurement of tilt angle by the autocollimation unit. Then, the laser is switched to output a beam with pulsed laser power in the term T_2 for the measurement of position by the rangefinder unit. The start of each measurement cycle shown in the figure as well as the switching from T_1 to T_2 are made by pushing the measurement button of the rangefinder manually. This is acceptable for the hand scraping and assembly processes since only static measurements are required.

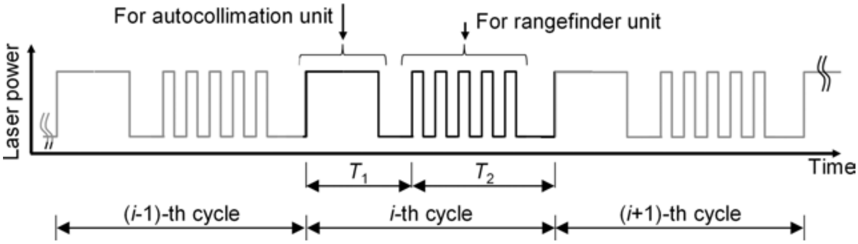

Fig. 1.38: Sequence of laser power control.

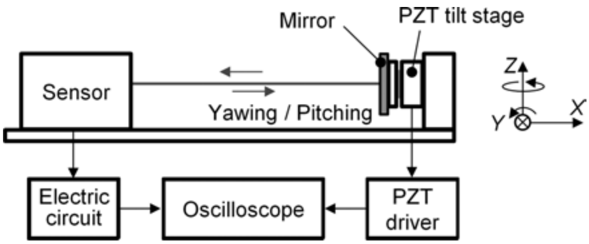

Fig. 1.39: Setup for testing the basic performances of the autocollimation unit.

The basic performances including the range, linearity and stability of the laser rangefinder-autocollimator were tested. Since the performance of the commercial rangefinder unit for position measurement has been reported by the manufacturer, the test was focused on the autocollimation unit for tilt angle measurement. Figure 1.39 shows the setup for the test. A PZT-driven 2D tilt motion stage was employed to generate the yaw ($\Delta\theta_Z$) and pitch ($\Delta\theta_Y$) tilt angles. A mirror was mounted on the tilt motion stage as the reflector for the autocollimation unit. The tilt angles of the stage were closed-loop controlled with strain gauges integrated into the stage. The initial tilt angles of the target mirror were adjusted to locate the center of the specular reflection beam from the reflector to that of the QPD.

Figures 1.40 and 1.41 show the 2D outputs of the autocollimation unit when tilt angles were applied to the mirror in the $\Delta\theta_Z$ and $\Delta\theta_Y$ directions, respectively. The distance x of the reflector was set to be 242 mm. It can be seen that a range of ±50 arc-seconds was achieved in the two directions. The linearity error of the output was within ±4.2 arc-seconds. The main reason for the nonlinearity was the non-uniform intensity distribution of the laser beam. The results of the short-term stability test are shown in Figs. 1.42 and 1.43, from which the resolution of the autocollimation unit can be indirectly evaluated. During the test, the reflector was kept stationary. The test term was set to 5 s. The stabilities were within 0.15 arc-second for $\Delta\theta_Z$ and 0.18 arc-second for $\Delta\theta_Y$, which implies the resolution of the autocollimation unit satisfied the requirements use in the hand scraping and assembly processes of precision linear slides.

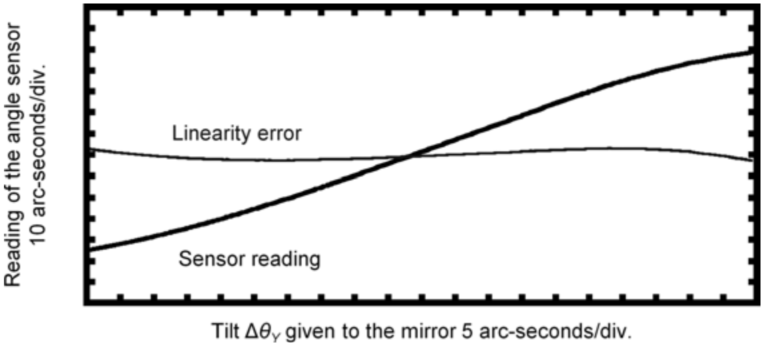

Fig. 1.40: Two-dimensional outputs of the autocollimation unit when tilt angles were applied to the reflector (L = 242 mm).

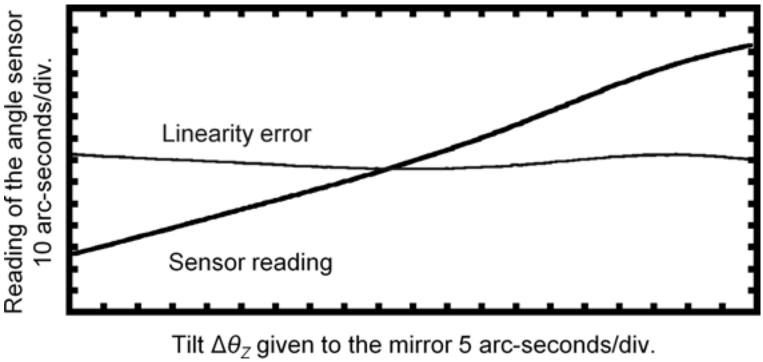

Fig. 1.41: Two-dimensional outputs of the autocollimation unit when tilt angles were applied to the reflector (L = 242 mm).

Figures 1.44 and 1.45 show the results of testing the cross-talk errors between the measurements of $\Delta\theta_Y$ and $\Delta\theta_Z$. A sinusoidal tilt angle motion was applied to the reflector by the PZT tilt motion stage along the direction of $\Delta\theta_Z$. The frequency and amplitude of the periodic tilt motion were 1 Hz and 50 arc-seconds, respectively. The outputs of the autocollimation unit in the two directions under this condition are shown in Fig. 1.44 where the cross-talk error in the direction of $\Delta\theta_Y$ was evaluated to

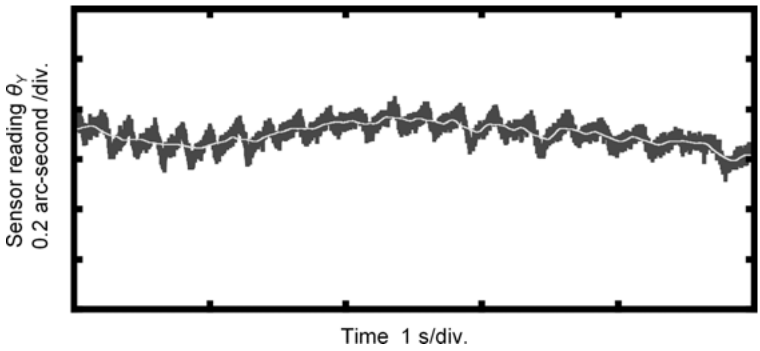

Fig. 1.42: Short-term stability of the autocollimation unit $\theta_{Y.}$

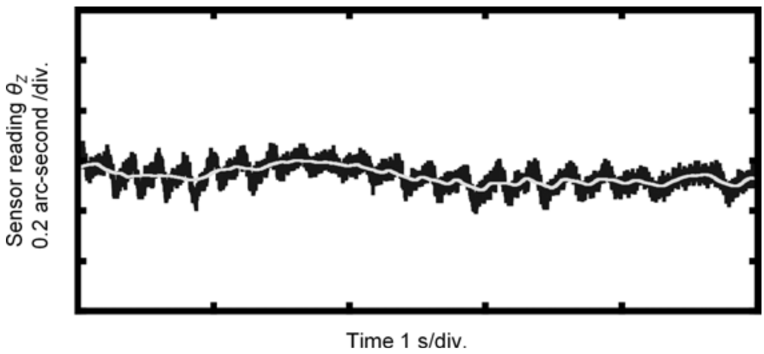

Fig. 1.43: Short-term stability of the autocollimation unit $\theta_{Z.}$

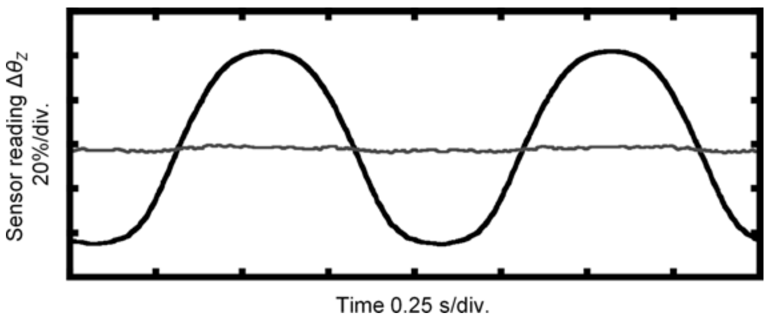

Fig. 1.44: Cross-talk errors of the autocollimation unit in $\Delta\theta_Y$.

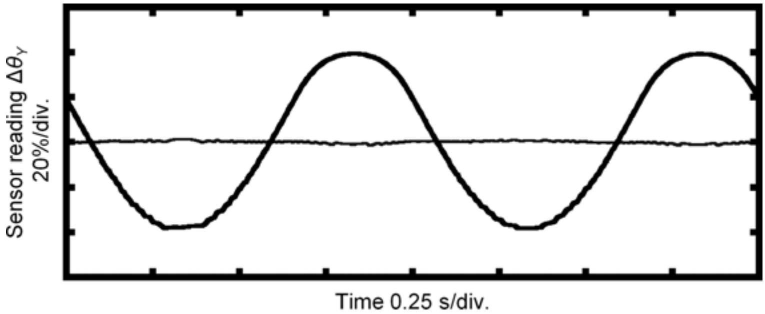

Fig. 1.45: Cross-talk errors of the autocollimation unit in $\Delta\theta_Z$.

be 1.8 arc-seconds. Then the sinusoidal tilt motion was applied in the direction of $\Delta\theta_Y$. The corresponding outputs are shown in Fig. 1.45 where the cross-talk error in the direction of $\Delta\theta_Z$ was evaluated to be 1.4 arc-seconds. The cross-talk errors were caused by the misalignment of the axes of the QPD.

The laser rangefinder was employed to measure a linear guide. The setup is shown in Fig. 1.46. A reflector was mounted on the stage plate of the linear guide. The axis of motion of the linear guide was set to be the X-axis. The measured pitch ($\Delta\theta_Y$) and yaw ($\Delta\theta_Z$) error motions are shown in Figs. 1.47 and 1.48, respectively. The position of the reflector at each measurement point was detected by the rangefinder unit. It can be seen from the figure that the yaw and pitch error motions were measured to be approximately 25 arc-seconds and 50 arc-seconds, respectively, over a movement distance of 110 mm along the X-direction.

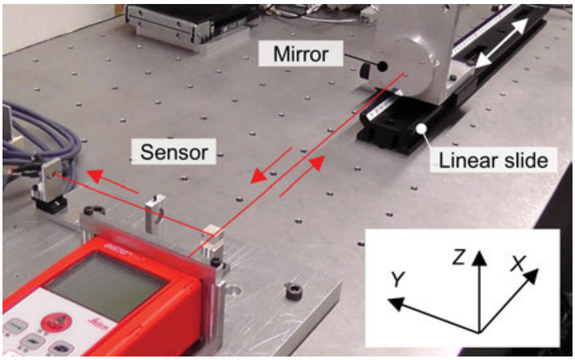

Fig. 1.46: Setup for measurement of a linear guide.

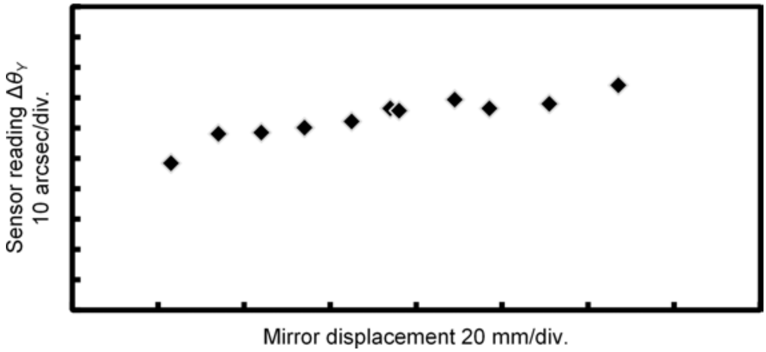

Fig. 1.47: Measured tilt error motions of a linear guide (yaw error $\Delta\theta_Y$).

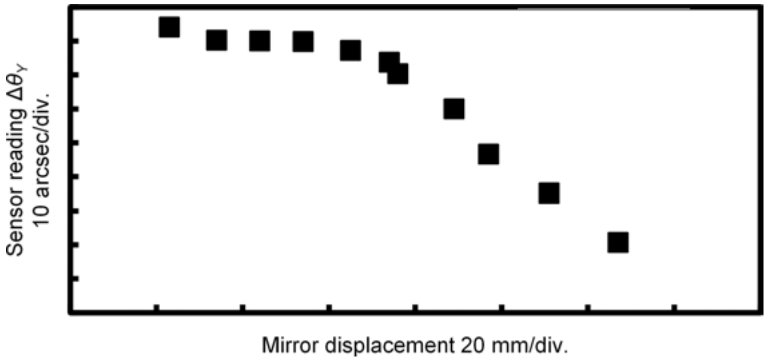

Fig. 1.48: Measured tilt error motions of a linear guide (pitch error $\Delta\theta_Z$).

1.4 PD-edge method associated with laser autocollimation

As presented in the previous sections, the sensitivity of laser autocollimation for angle measurement is significantly influenced by the diameter of the laser beam focused on the PD cell. In addition, with the increasing use of lasers in research laboratories and machine shops for measurement and materials processing, evaluation of the diameter of a small focused laser beam is getting more important for the assurance of product quality and/or fabrication resolution. A simple and cost-effective method for diameter measurement of a focused laser beam is thus required.

The knife-edge method [41–43] is the most well used method for beam diameter measurement. Figure 1.49 shows a schematic of the knife-edge method. In this method, a knife-edge is made to scan across the laser beam. The beam diameter is evaluated by reconstructing the intensity distribution of the beam by measuring the optical powers passed through the knife-edge during the scanning. On the other hand, the influence of light diffraction occurring at the knife-edge becomes more significant as the decrease of the laser beam diameter, which cannot be neglected where the photodetector is placed at a certain distance from the knife-edge. As shown in Fig. 1.50, this problem can be overcome by placing a thin-film structure, known as a knife pad [44–47], right above the PD cell in a photodetector. However, a precise knife pad is required for this method, which is not easy for ordinary research laboratories and machine shops. In addition, the measurement of a focused laser beam can be influenced by the thickness of the knife pad. The measurement is also influenced by the positioning errors and motion errors of the linear scanning mechanism for moving the knife in the knife-edge method or the knife pad and the photodetector in the knife-pad method.

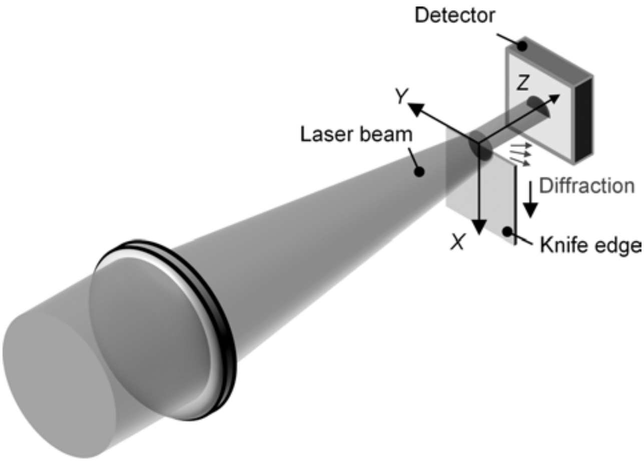

Fig. 1.49: The knife-edge method for diameter measurement of a focused laser beam.

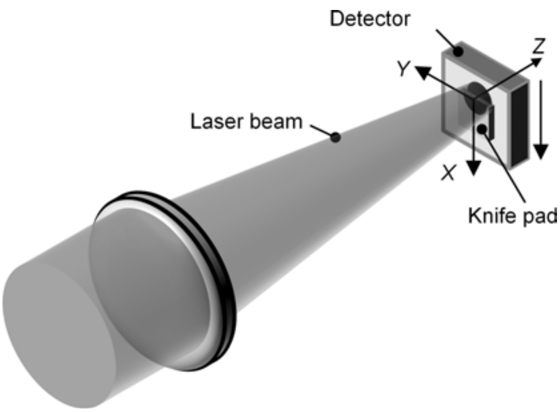

Fig. 1.50: The knife-pad method.

In this section, a new method referred to as the PD-edge method is presented. The method associated with laser autocollimation can make diameter measurement of a focused laser beam diameter in a simple and cost-effective manner [21]. Assume the center axis of the focused laser beam with a diameter of d is aligned to coincide with the Z-axis. The light intensity distribution $I(x,y)$ in the focal plane (XY-plane) of the focusing lens can be expressed by a Gaussian function as follows [29]:

$$I(x,y) = I_0 \exp\left(-\frac{2(x^2+y^2)}{(d/2)^2}\right) \tag{1.23}$$

where (x,y) is the coordinates in the focal plane and I_0 is the light intensity at the center axis of the laser beam. d is the diameter where $I(x,y)$ decreases to $1/e^2$ of I_0. Denoting the X-position of the knife-edge in Fig. 1.50 by x', the total power of the laser beam $P(x')$ passing through the knife edge can be calculated as follows:

$$P(x') = \int_{-\infty}^{x'} \int_{-\infty}^{\infty} I(x,y)dydx \tag{1.24}$$

Meanwhile, the total power of the whole laser beam P_0 can be calculated by:

$$P_0 = \int_{-\infty}^{\infty} \int_{-\infty}^{\infty} I(x,y)dydx = \frac{\pi I_0 d^2}{8} \tag{1.25}$$

$\overline{P(x')}$, which corresponds to $P(x')$ normalized by P_0 can therefore be obtained as:

$$\overline{P(x')} = \frac{P(x')}{P_0} = \frac{8}{\pi I_0 d^2} \int_{-\infty}^{x'} \int_{-\infty}^{\infty} I(x,y)dydx \tag{1.26}$$

By making the knife edge to scan over the laser beam to obtain $\overline{P(x')}$ and taking the derivative of $\overline{P(x')}$ with respect to x', $I(x,y)$ can be reconstructed [18, 41, 42], from which d can be evaluated.

Figure 1.51 shows a schematic of the PD-edge method for diameter measurement of a focused laser beam. The edge of a PD is employed as the knife edge and the PD itself is employed as the photodetector. The beam diameter can be measured by moving the PD along the X-direction so that the PD-edge can scan across the focused light spot. Since the knife-edge and the detector surface are one component and on the same plane, the problems inherent in the conventional knife-edge method and the knife-pad method can be solved. In addition, taking into consideration the PD is located at the focal plane of the focusing lens, the combination of the PD and the lens can be regarded as a laser autocollimation unit where the focusing lens functions as a CO. Based on the principle of laser autocollimation, a θ_Y-directional tilt motion of the beam incident to the lens will be converted into a linear motion of the focused light spot along the X-direction. Therefore, the linear scan motion necessary for the diameter measurement of the focused light spot can be easily generated by a rotary or a tilt stage in a cost-effective way as shown in Fig. 1.51.

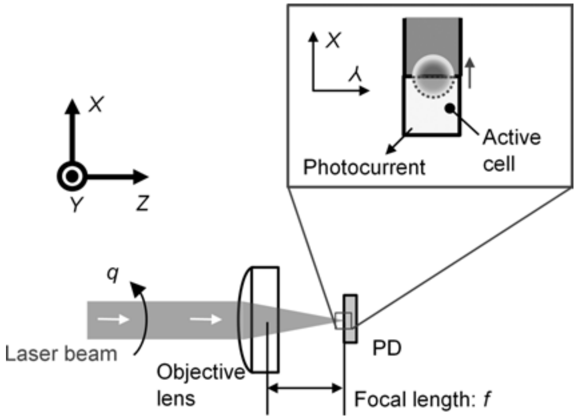

Fig. 1.51: A setup for the PD-edge method.

Assume that the PD–edge is located at the center of the focused light spot when the angular displacement $\Delta\theta_Y$ of the mirror reflector is zero. The change in the total power of the irradiated laser beam ΔP with respect to $\Delta\theta_Y$ (=$\Delta\phi/2$) can be expressed by

$$\begin{aligned}\Delta P &= \int_{-\infty}^{f\tan 2\Delta\theta}\int_{-\infty}^{\infty} I(x,y)dydx - \int_{-\infty}^{0}\int_{-\infty}^{\infty} I(x,y)dydx \\ &\approx (f\tan 2\Delta\theta)\cdot\int_{-\infty}^{\infty} I_0\exp\left(\frac{-8y^2}{d^2}\right)dy \approx 2f\Delta\theta\int_{-\infty}^{\infty} I_0\exp\left(\frac{-8y^2}{d^2}\right)dy \\ &= \sqrt{\frac{\pi}{2}}I_0 df\Delta\theta\end{aligned} \tag{1.27}$$

where f is the focal length of the focusing lens. From eqs. (1.25) and (1.27), $\overline{\Delta P}$, which corresponds to ΔP normalized by the total power of the whole laser beam P_0, can be obtained as follows:

$$\Delta\overline{P} = \sqrt{\frac{\pi}{2}}I_0 df\Delta\theta \bigg/ \frac{\pi I_0 d^2}{8} = \sqrt{\frac{2}{\pi}}\frac{4f}{d}\Delta\theta \tag{1.28}$$

By denoting the gradient of $\overline{\Delta P}$ with respect to $\Delta\theta_Y$ as S (=$\overline{\Delta P}/\Delta\theta$), eq. (1.28) can be modified as follows:

$$d \approx \frac{4\sqrt{2}f}{\sqrt{\pi}S} \tag{1.29}$$

where the relationship between d and S is obtained. As can be seen in the equation, since f is a known parameter in the setup, d can be estimated by S.

Figure 1.52 shows typical photodetector outputs with respect to the linear scan positions in the conventional knife-edge/knife-pad methods. For the conventional methods, the photodetector output, which is a function of the displacement of a knife-edge/knife-pad, is required to be monitored over a scan range across most of the focused light spot for the evaluation of d. Figure 1.53 shows the outputs of the PD-edge method with respect to the angular position of the reflector. Since d is evaluated from the gradient S of the output curve in a small angular range $\Delta\theta$, the tilt scan range of the reflector can be very small, which is an advantage of the PD-edge method.

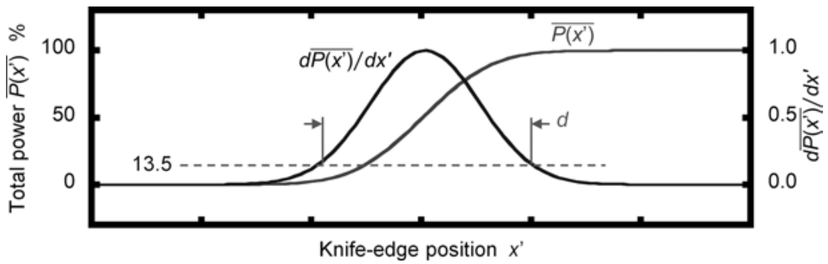

Fig. 1.52: Outputs of the conventional methods for beam diameter measurement.

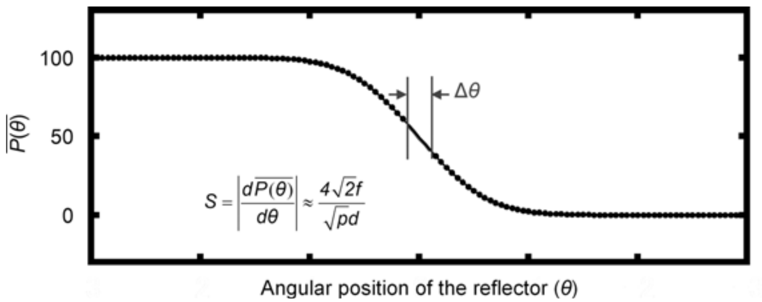

Fig. 1.53: Output of the PD-edge method for beam diameter measurement.

An experimental setup shown in Figure 1.54 was built to test the characteristics of a commercial PD, specifically the sensitivity to input optical power around its edge area. A picture of the setup is shown in Fig. 1.55. A LD with a wavelength λ of 685 nm and a maximum laser power of 70 mW was employed as the light source. The light rays emitted from the LD were collimated by an aspheric lens to form a collimated laser beam. The beam was then expanded to a large beam with a diameter of approximately 26 mm by using a beam expander. The expanded collimated laser beam was made to focus on the edge of one of two cells of the bi-cell PD (S4202, Hamamatsu photonics). An optical microscopic image of the bi-cell PD is shown in Fig. 1.56. The PD was mounted on an X-directional linear slide whose displacement was measured by a length gauge. As shown in Fig. 1.56, three edges (A, B, C) of the right-side PD were tested. Edge-A is the edge adjacent to the neighboring the left-side PD and Edge-C is the conjugating edge between the active cell and the electrode. Edge-B is an independent edge. The length of each of the edges was 1 mm.

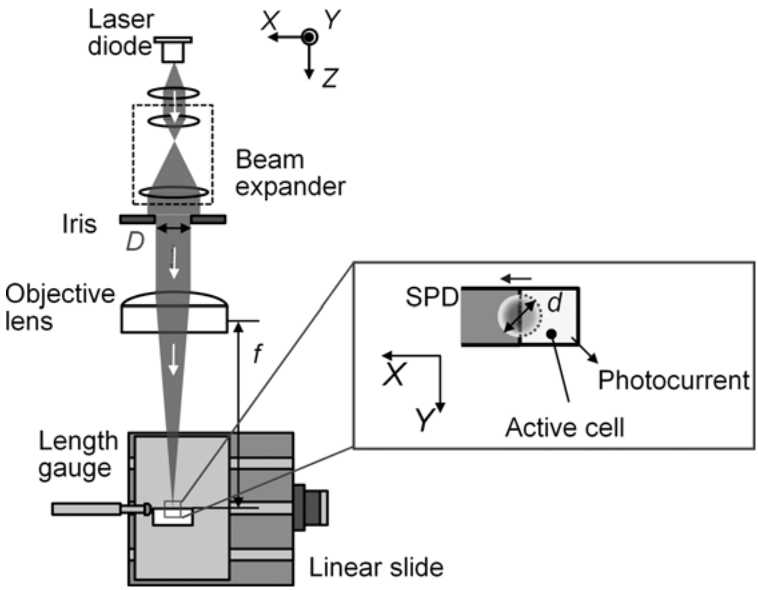

Fig. 1.54: An experimental setup for testing the characteristics of PD-edges.

In testing of Edge-A and Edge-C, the PD was moved along the X-direction in a step of 10 μm to scan across the focused laser beam. The focused beam was kept stationary and its diameter d was approximately 130 μm. During the scan, a photocurrent from the PD at each X-position was recorded. The photocurrent was converted into a voltage output, referred to as the PD output, by using a transimpedance circuit. For testing Edge-B, it was necessary to rotate the PD holder 90°. Figure 1.57 shows the PD output curves in the testing of the edge. As can be seen in the figure, Edge-C was most sensitive to the PD displacement, indicating that Edge-C was most proper for use in the PD-edge method as well as the knife-pad method of beam diameter measurement.

Edge-C of the PD was first applied to the conventional knife-pad method in the setup shown in Figs. 1.54 and 1.55. During the measurement, the PD was moved along the X-direction with a constant velocity of 5 μm/s. The PD output and the length gauge output were acquired simultaneously during the scan. The measurement results are shown in Fig. 1.58. By taking the derivative of the PD output with

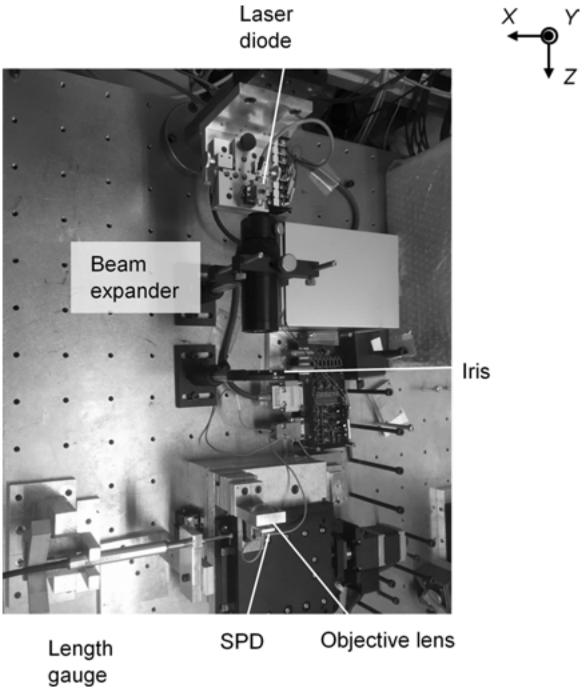

Fig. 1.55: Picture of the setup in Fig. 1.43.

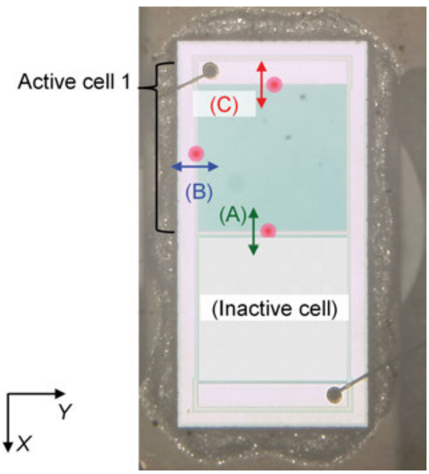

Fig. 1.56: A microscope image of the PD and the edges for test.

respect to the X-position of the PD, the intensity distribution of the focused laser beam was reconstructed in the figure, from which the diameter of the focused laser beam, which was denoted by d_{knife}, could be evaluated based. As shown in Figs. 1.54 and 1.55, a diameter-variable iris was placed between the beam expander

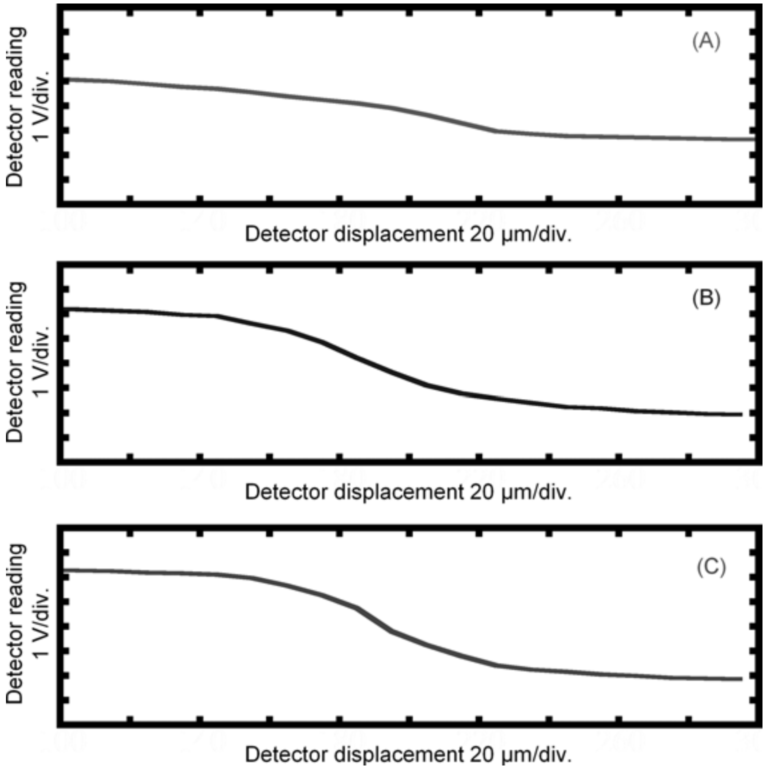

Fig. 1.57: PD output curves in the testing of the edges.

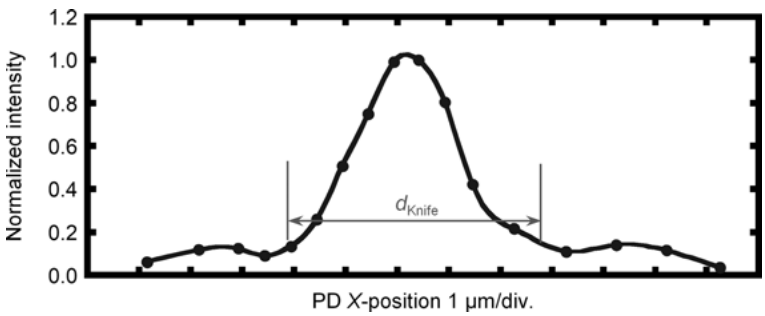

Fig. 1.58: Measurement results by the knife-pad method with Edge-C.

and the objective lens for adjusting the diameter D_0 of the collimated laser beam before it was made incident to the objective lens.

Edge-C of the PD was then applied to the PD-edge method in the setup shown in Fig. 1.59. A picture of the setup is shown in Fig. 1.60. The optical components including the laser source, the beam expander and the diameter-variable iris were the same as those in Fig. 1.55. A reflector mounted on a PZT tilt stage was employed to tilt the collimated laser beam with a diameter D_0 about the Y-axis. The laser beam from the reflector was focused on the PD for the diameter measurement. The PD was mounted on a manual three-axis positioning stage. The collimated laser beam was divided into two beams by using a BS. One beam was received by a reference PD for monitoring the light intensity deviation of the laser source. The other beam was employed for the diameter measurement where the center of the focused laser beam was positioned on Edge-C of the PD when the PZT tilt stage was at the initial angular position.

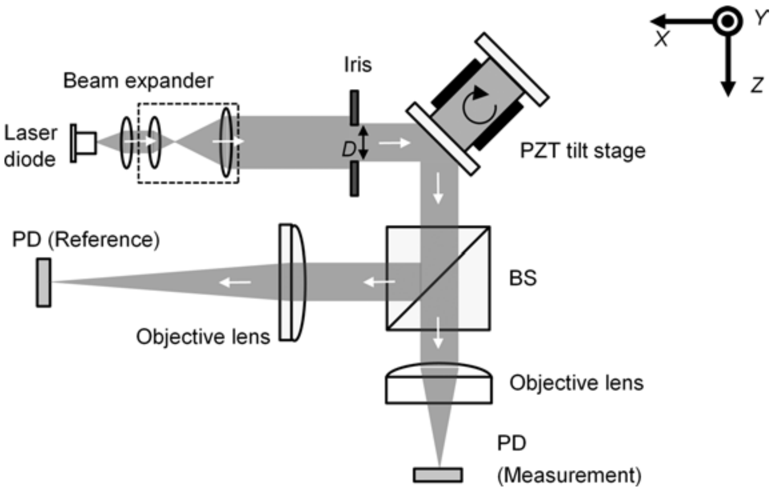

Fig. 1.59: Experimental setup for the PD-edge method of beam diameter measurement.

A small angular displacement $\Delta\theta$ of ±1 arc-second was applied to the reflector by using the PZT tilt stage while the PD output was acquired, from which the gradient S of the PD output can be evaluated. The ±1 arc-second angular displacement of the reflector corresponded to a ±0.17 μm linear displacement of the focused laser beam on the PD. D_0 was changed by using the diameter-variable iris from 1 to 10 mm. The evaluated S at each D_0 is shown in Fig. 1.61. As can be seen in the figure, S increased with the increase of D_0. As shown in eq. (1.29), an increase in S corresponded to a decrease in the measured diameter of the focused laser beam by the PD-edge method, which was referred to as d_{edge}. The evaluated d_{edge} based on eq. (1.29) at each D_0 was also plotted in Fig. 1.61. d_{edge} by the PD-edge method and d_{knife} by the knife-pad method are compared in Fig. 1.62. A good agreement can be found between the results by the two different methods. This verified advantage in the PD-method, that is, the gradient S acquired within a narrow range is effective enough for the accurate evaluation of the focused laser beam diameter.

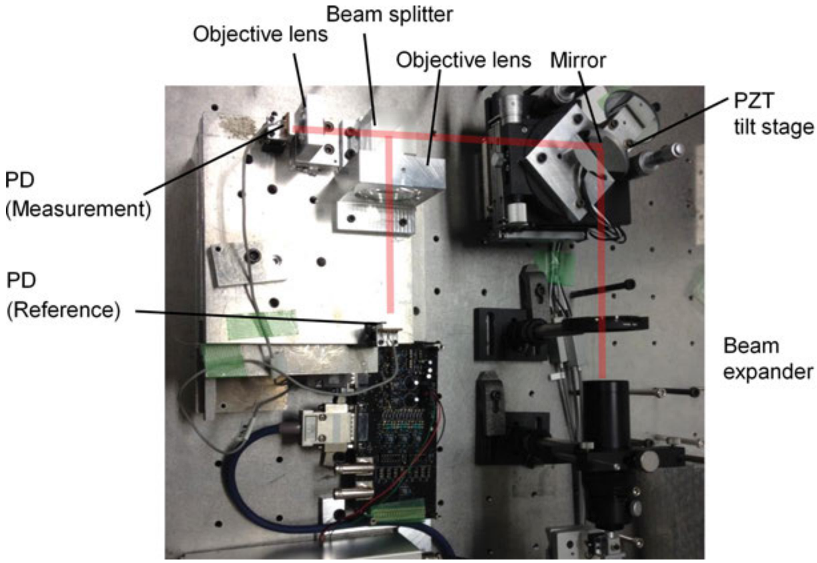

Fig. 1.60: A picture of the setup shown in Fig. 1.48.

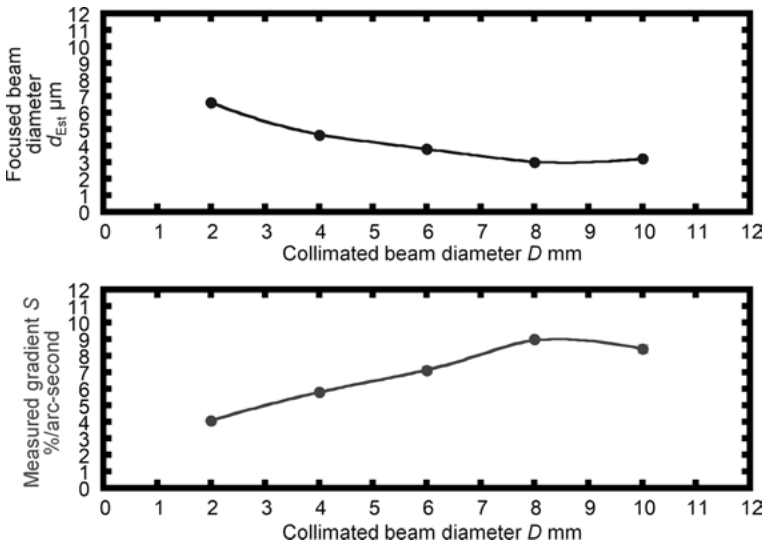

Fig. 1.61: Measured S and d_{edge} by the PD-edge method.

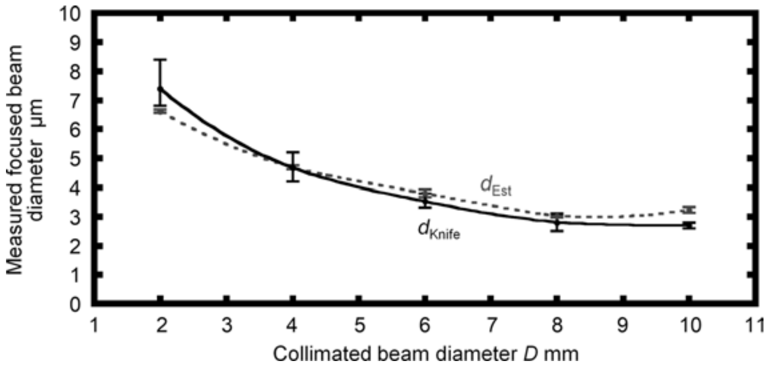

Fig. 1.62: Comparison between the measured beam diameters by the PD-edge method and the Knife-pad method.

1.5 Summary

A laser rangefinder-autocollimator has been presented for the hand scraping process and the assembly process of slide stages. The 2D tilt angle components (pitch and yaw) of a reflector were mounted on the guideways or those of the moving carriage of the stage while providing the position information of the reflection for the necessary operations in the processes. The angle measurement and the position measurement are based on the laser autocollimation method and the time-of-flight method, respectively. A commercial rangefinder with a resolution of 1 mm and a range of 30 m has been chosen as the rangefinder unit. A laser autocollimation unit has been designed to integrate with the rangefinder unit. Geometrical models have been established for designing the diameter and focal length of the CO as well as the size of the BS used in the autocollimation unit. The laser rangefinder-autocollimator had a size of 250 mm (X) × 205 mm (Y) × 63 mm (Z). The performances of the autocollimation unit, including sensitivity, stability, linearity, measurement range as well as cross-talk error have been investigated. It has been verified that the constructed laser rangefinder-autocollimator could satisfy the design goals of measurement resolutions and ranges.

A nanoradian laser autocollimator with a compact size of 100 mm (X) × 150 mm (Y) has then been presented for ultrasensitive tilt angle measurement of precision linear stages. Influences of the spherical aberration of CO on the sensitivity of laser autocollimation have been investigated by computer simulation based on wave optics. The simulation results have revealed that the increase of the measurement laser beam diameter D_0 is effective in improving the autocollimator sensitivity when D_0 is smaller than 10 mm where the influence of the spherical aberration is insignificant. In the measurement experiment, the measured focused light spot diameter and the measured autocollimator sensitivity had a good agreement with the simulation results. The designed and constructed nanoradian laser autocollimator has reached a resolution of 0.001 arc-second (4.8 nrad) with a measurement laser beam diameter D_0 of 5 mm.

A new PD-edge method associated with laser autocollimation has been presented for diameter measurement of a focused laser beam diameter. In this method, the lens for focusing the laser beam is treated as the CO in an autocollimation unit. The focused laser beam is aligned on the PD cell edge of a photodiode, which is located at the focal position of the focusing lens. A small angular displacement $\Delta\phi$ is given to a collimated laser beam before being made incident to the lens. The angular displacement of the collimated laser beam will generate a linear scan motion of the focused laser beam across the PD-edge. The output of the photodiode during the scan is acquired to obtain the gradient S of the PD output, from which the diameter of the focused laser beam diameter d can be evaluated. It has been verified that a commercial photodiode can be utilized for the PD-edge method. Experimental results have demonstrated the feasibility of the PD-edge method for diameter measurement of micrometric focused laser beams.

References

[1] Gao W, Haitjema H, Fang FZ, Leach RK, Cheung CF, Savio E, Linares JM. On-machine and in-process surface metrology for precision manufacturing. CIRP Ann 2019, 68, 2, 843–866.

[2] Buice ES, Otten D, Yang RH, Smith ST, Hocken RJ, Trumper DL. Design evaluation of a single-axis precision controlled positioning stage. Precis Eng 2009, 33, 4, 418–424.

[3] Gao W, Arai Y, Shibuya A, Kiyono S, Park CH. Measurement of multi-degree-of-freedom error motions of a precision linear air-bearing stage. Precis Eng 2006, 30, 1, 96–103.

[4] Oiwa T, Katsuki M, Karita M, Gao W, Makinouchi S, Sato KOY. Report of questionnaire survey on ultra-precision positioning; technical committee of ultra-precision positioning. Japan Soc Precis Eng Tokyo, Japan 2016, 81, 10, 904–910.

[5] Gao W, Kim SW, Bosse H, Haitjema H, Chen YL, Lu XD, Knapp W, Weckenmann A, Estler WT, Kunzmann H. Measurement technologies for precision positioning. CIRP Ann – Manuf Technol 2015, 64, 2, 773–796.

[6] Moore WR, Special M, Co T. Foundations of Mechanical Accuracy. 1970.

[7] Hwang J, Park C-H, Gao W, Kim S-W. A three-probe system for measuring the parallelism and straightness of a pair of rails for ultra-precision guideways. Int J Mach Tools Manuf 2007, 47, 7–8, 1053–1058.

[8] Fan K-C, Torng J, Jywe W, Chou R-C, Ye J-K. 3-D measurement and evaluation of surface texture produced by scraping process. Measurement 2012, 45, 3, 384–392.

[9] Seiki M. Topics about "Scraping." (Accessed March 16, 2021, at http://www.mitsuiseiki.co.jp/machine/tabid/192/Default.aspx)

[10] Kunzmann H, Pfeifer T, Flügge J. Scales vs. Laser Interferometers Performance and Comparison of Two Measuring Systems. CIRP Ann – Manuf Technol 1993, 42, 2, 753–767.

[11] Zhang JH, Menq CH. A linear/angular interferometer capable of measuring large angular motion. Meas Sci Technol 1999, 10, 12, 1247–1253.

[12] Kimura A, Gao W, Kim W, Hosono K, Shimizu Y, Shi L, Zeng L. A sub-nanometric three-axis surface encoder with short-period planar gratings for stage motion measurement. Precis Eng 2012, 36, 4.

[13] Li X, Gao W, Muto H, Shimizu Y, Ito S, Dian S. A six-degree-of-freedom surface encoder for precision positioning of a planar motion stage. Precis Eng 2013, 37, 3, 771–781.
[14] Jang Y-S, Kim S-W. Distance measurements using mode-locked lasers: A review. Nanomanufacturing Metrol 2018, 1, 3, 131–147.
[15] Ennos AE, Virdee MS. High accuracy profile measurement of quasi-conical mirror surfaces by laser autocollimation. Precis Eng 1982, 4, 1, 5–8.
[16] Saito Y, Gao W, Kiyono S. A single lens micro-angle sensor. Int J Precis Eng Manuf 2007, 8, 2, 14–18.
[17] Gao W, Saito Y, Muto H, Arai Y, Shimizu Y. A three-axis autocollimator for detection of angular error motions of a precision stage. CIRP Ann – Manuf Technol 2011, 60, 1, 515–518.
[18] Shimizu Y, Tan SL, Murata D, Maruyama T, Ito S, Chen Y-L, Gao W. Ultra-sensitive angle sensor based on laser autocollimation for measurement of stage tilt motions. Opt Express 2016, 24, 3, 2788.
[19] Tan SL, Shimizu Y, Meguro T, Ito S, Gao W. Design of a laser autocollimator -based optical sensor with a rangefinder for error correction of precision slide guideways. Int J Precis Eng Manuf 2015, 16, 3, 423–431.
[20] Murata D An ultra-sensitive optical angle sensor. Tohoku University, Master thesis, 2014.
[21] Shimizu Y, Maruyama T, Nakagawa S, Chen Y-LY-L-L, Matsukuma H, Gao W. A PD-edge method associated with the laser autocollimation for measurement of a focused laser beam diameter. Meas Sci Technol 2018, 29, 7, 0–6.
[22] Maruyama T An ultra-high sensitive optical angle sensor. Tohoku University, Master thesis, 2016.
[23] Keysight Technologies. Keysight Technologies 55280B Linear Measurement Kit Data Sheet Optical Setup for Linear Measurements Basic Equipment. (Accessed November 18, 2020, at www.keysight.com/find/5530)
[24] MÖLLER-WEDEL OPTICAL. Electroninc autocollimator. (Published 2007 Accessed March 14, 2021, at www.moeller-wedel-optical.com)
[25] Newport. CONEX-LDS Electronic Autocollimator. (Accessed November 18, 2020, at https://www.newport.com/f/conex-lds-electronic-autocollimator)
[26] Saito Y, Arai Y, Gao W. Investigation of an optical sensor for small tilt angle detection of a precision linear stage. Meas Sci Technol 2010, 21, 5, 054006.
[27] Gao W. Precision Nanometrology. London, Springer London, 2010.
[28] Bennett SJ, Gates JWC. The design of detector arrays for laser alignment systems. J Phys E 1970, 3, 1, 65–68.
[29] Hecht E. Optics. 5th Pearson, 2017.
[30] Smith JW. Modern Optical Engineering. McGraw Hill, 2007.
[31] Goodman JW. Introduction to Fourier Optics. Roberts & Company, 2004.
[32] Mahajan VN Optical imaging and aberrations. 1000 20th Street, Bellingham, WA 98227-0010 USA, SPIE, 1998.
[33] Otsuka J, Ichikawa S, Masuda T, Suzuki K. Development of a small ultraprecision positioning device with 5 nm resolution. Meas Sci Technol 2005, 16, 11, 2186–2192.
[34] Bryan JB. The Abbé principle revisited: An updated interpretation. Precis Eng 1979, 1, 3, 129–132.
[35] Meguro T, Shimizu Y, Gao W An angle sensor with a laser rangefinder. Proceedings of International Conference on Leading Edge Manufacturing in twenty-first Century: LEM21, The Japan Society of Mechanical Engineers, 2011, 1–4.
[36] Ennos AE, Virdee MS. High accuracy profile measurement of quasi-conical mirror surfaces by laser autocollimation. Precis Eng 1982, 4, 1, 5–8.

[37] Gueuning F, Varlan M, Eugene C, Dupuis P Accurate distance measurement by an autonomous ultrasonic system combining time-of-flight and phase-shift methods. Conference Record – IEEE Instrumentation and Measurement Technology Conference, Vol 1. IEEE, 1996, 399–404.

[38] Amann M-C, Bosch T, Marc L, Risto M, Marc R. Laser ranging: a critical review of usual techniques for distance measurement. Opt Eng 2001, 40, 1, 10.

[39] Leica Geosystems. DISTO Lite5 User Manual. (Accessed November 18, 2020, at https://shop.leica-geosystems.com/sites/default/files/2019-03/leica_disto_lite5_en.pdf)

[40] Saito Y, Arai Y, Gao W. Detection of three-axis angles by an optical sensor. Sensors Actuators, A Phys 2009, 150, 2, 175–183.

[41] Arnaud JA, Hubbard WM, Mandeville GD, De La Clavière B, Franke EA, Franke JM. Technique for Fast Measurement of Gaussian Laser Beam Parameters. Appl Opt 1971, 10, 12, 2775.

[42] Suzaki Y, Tachibana A. Measurement of the µm sized radius of Gaussian laser beam using the scanning knife-edge. Appl Opt 1975, 14, 12, 2809.

[43] Firester AH, Heller ME, Sheng P. Knife-edge scanning measurements of subwavelength focused light beams. Appl Opt 1977, 16, 7, 1971.

[44] Dorn R, Quabis S, Leuchs G. Sharper focus for a radially polarized light beam. Phys Rev Lett 2003, 91, 23, 233901.

[45] Huber C, Orlov S, Banzer P, Leuchs G. Corrections to the knife-edge based reconstruction scheme of tightly focused light beams. Opt Express 2013, 21, 21, 25069.

[46] Huber C, Orlov S, Banzer P, Leuchs G. Influence of the substrate material on the knife-edge based profiling of tightly focused light beams. Opt Express 2016, 24, 8, 8214.

[47] Marchenko P, Orlov S, Huber C, Banzer P, Quabis S, Peschel U, Leuchs G. Interaction of highly focused vector beams with a metal knife-edge. Opt Express 2011, 19, 8, 7244.

Chapter 2
Three-axis angle sensor

2.1 Introduction

Precision positioning of a machining tool or a measuring probe is a common operation in precision engineering, in which a linear stage is employed for one-axis applications or a combination of multiple linear stages is employed for two- or three-axis applications [1–3]. As shown in Fig. 2.1, such a precision linear stage is typically equipped with a position sensor, often a linear encoder or a laser interferometer, for closed-loop control of the stage along its axis of motion. It is necessary to align the measuring axis of the position sensor coaxially with the axis of motion of the stage to avoid the Abbe error caused by angular error motions of the stage [4–6]. The positioning systems for ultraprecision metrological applications, such as the line scale comparator and the metrological scanning probe microscope, are basically designed to obey the Abbe principle [7, 8]. Many other positioning systems, such as those for machine tools and coordinate measuring machines (CMMs), however, do not satisfy the Abbe principle [9]. In such a system, the position of the machining tool or the measuring probe has a certain distance from the axis of the position sensor, which is called the Abbe offset.

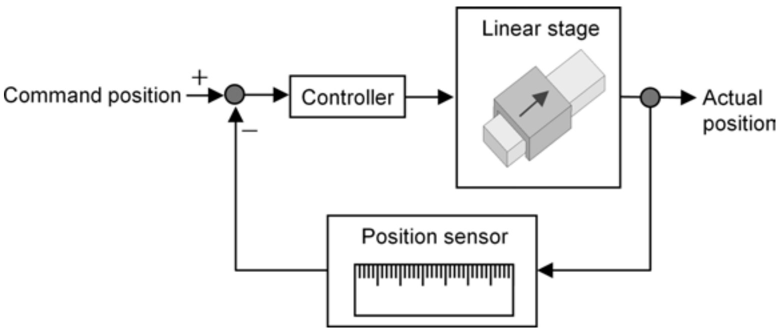

Fig. 2.1: Closed-loop control of a linear stage.

Even a small angular motion of the linear stage could cause a large amount of Abbe error if the Abbe offset is large. Figure 2.2 shows a commercial ultraprecision linear stage driven by a linear motor. A linear encoder with a resolution of 0.14 nm is employed as the position sensor for closed-loop control. In this example, the Abbe offset is approximately 100 mm. As shown in Fig. 2.3, in this case, an angular motion with an amplitude of 1 arc-second will generate an Abbe error with an amplitude of 0.48 µm. Taking into consideration the amplitude of the angular error motion of a precision stage is typically larger than 1 arc-second [10] and most of the precision

https://doi.org/10.1515/9783110542363-002

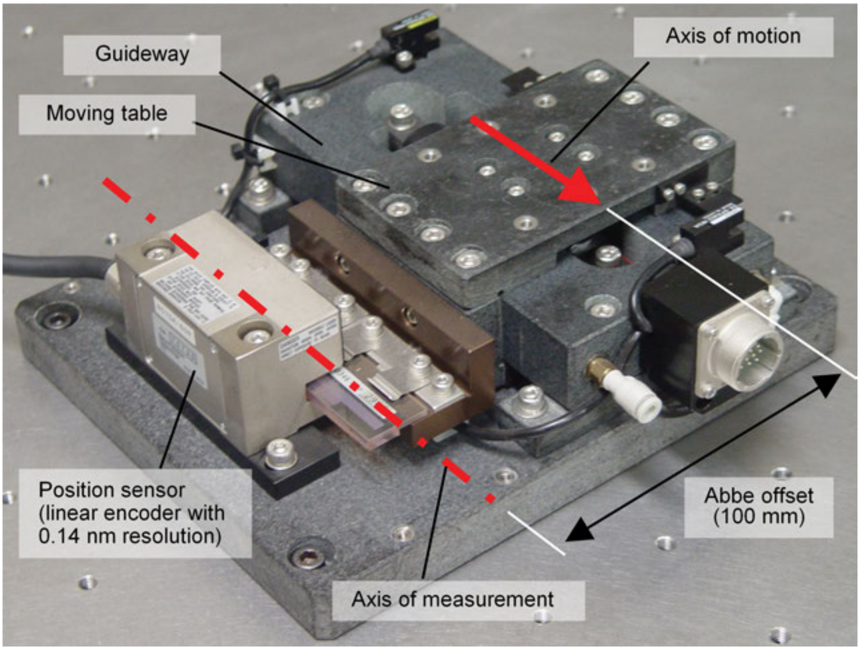

Fig. 2.2: Abbe offset in a commercial ultraprecision air-bearing linear stage.

stages are required to have a positioning precision better than 0.1 μm, the Abbe error is a large error factor for the precision stage. Detection of the angular error motion of the stage is thus important for evaluation and compensation of the Abbe error.

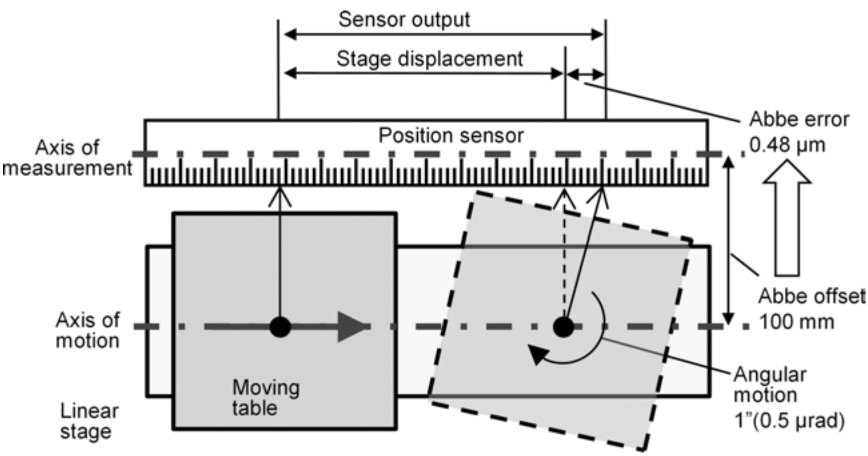

Fig. 2.3: Influence of the Abbe error on positioning accuracy.

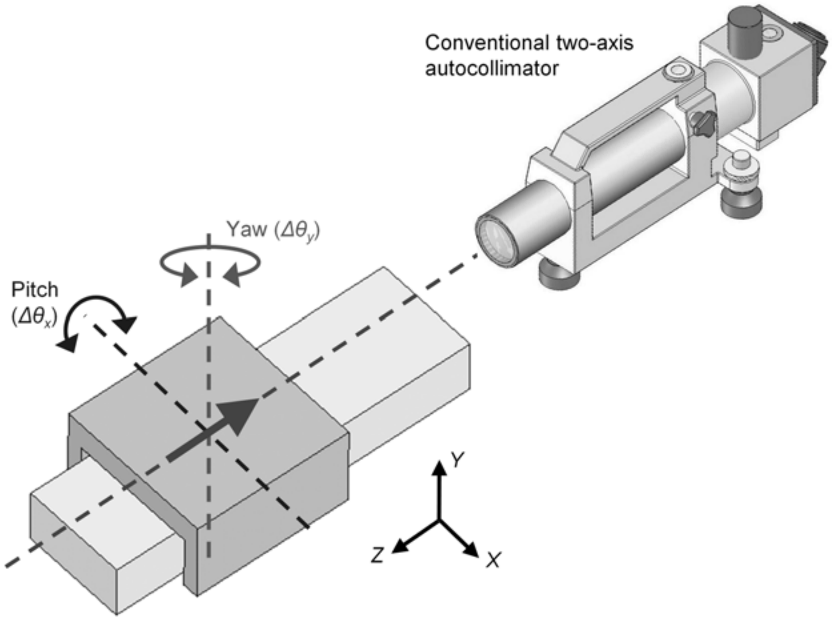

Fig. 2.4: Pitch and yaw two-axis measurement by a conventional autocollimator.

Assuming that the stage travels along the Z-axis, the pitch, yaw and roll errors are the components of the angular error motion about the X-, Y- and Z-axes, respectively. As shown in Fig. 2.4, a conventional autocollimator [11] can be used to detect the pitch error ($\Delta\theta_x$) and yaw error ($\Delta\theta_y$) of the linear stage [10, 12]. Figure 2.5 shows a schematic of the autocollimator. In the detection, a light beam from the autocollimator is projected onto a flat mirror reflector along the surface normal of the mirror, which is mounted on the stage moving table. The reflected beam from the flat mirror reflector is received by the autocollimation unit, which consists of a collimator objective and a two-directional light position-sensing detector placed at the focal plane of the collimator objective [13, 14]. As presented in the previous chapter, based on the principle of autocollimation, the pitch and yaw errors will be converted into Y- and X-directional linear displacements of the light spot on the detector (Δy, Δx), respectively, from which the pitch and yaw errors can be simultaneously detected. Commercial autocollimators can achieve a high resolution of 0.01 arc-second. However, the roll error ($\Delta\theta_z$) cannot be detected by conventional autocollimators because the reflected beam from the flat mirror reflector does not respond to the rotational motion about the surface normal of the flat mirror reflector.

This chapter presents a three-axis angle sensor that can simultaneously detect the three-axis components of the angular error motion of a precision linear stage (Fig. 2.6). In such a three-axis angle sensor, the flat mirror used in the conventional two-axis autocollimator is replaced with a refractive grating reflector. The diffracted beams reflected from the grating reflector are detected by a sensor head for the three-axis angle measurement [15–22]. Since the working distance between the sensor head and the reflector/moving table along the Z-direction varies with the movement of the moving table, the sensor is referred to as the variable working distance type. A constant working distance type sensor head is then presented for extending the detectable moving stroke of the linear stage. A three-axis inclination sensor [23, 24] is also presented.

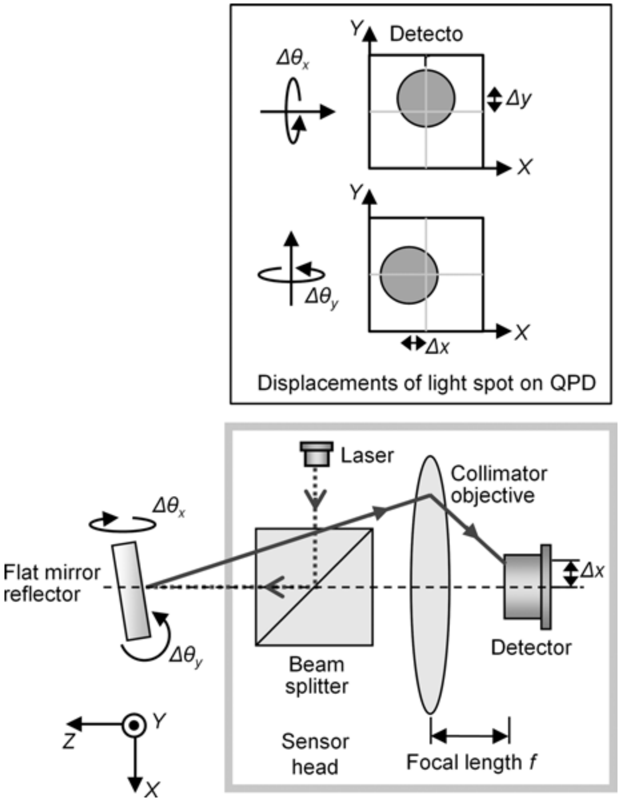

Fig. 2.5: Schematic of a conventional two-axis autocollimator.

2.2 Three-axis angle sensor

Figure 2.7 shows the concept for three-axis angle measurement. Compared with a conventional two-axis autocollimator shown in Fig. 2.5, a diffractive grating reflector is employed to replace the flat mirror reflector. In addition to the zeroth-order diffracted beam, the positive and negative first-order diffracted beams from the grating reflector are also received by the collimator objective. Three detectors are employed

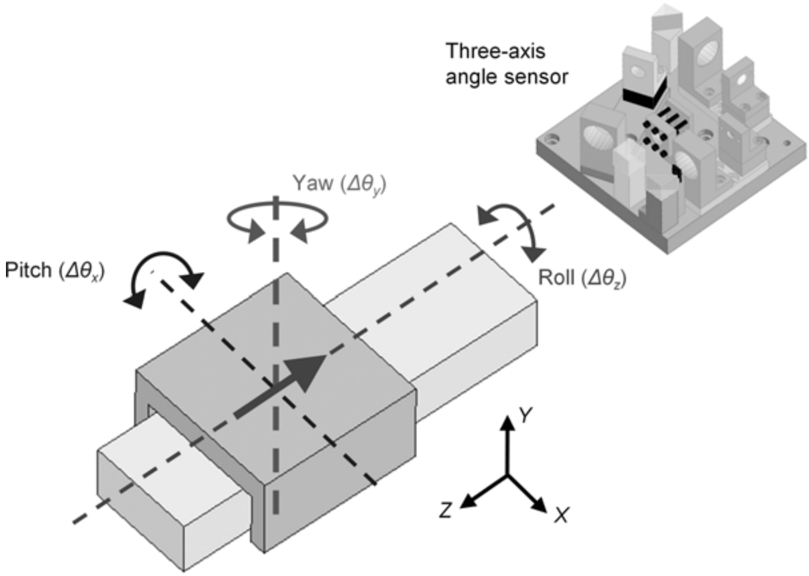

Fig. 2.6: Simultaneous measurement of pitch, yaw and roll errors by a three-axis angle sensor.

to detect the displacements of the focused diffracted beams on the focal plane of the collimator objective associated with the pitch, yaw and roll angular motions. Figure 2.8 shows the displacements of diffraction light spots focused on the detectors located at the focal plane of the collimator objective. As shown in the figure, if a pitch angle $\Delta\theta_x$ is applied to the grating reflector, it will generate the same amount of linear displacement on the three detectors along the Y-direction, which is the same as the conventional two-axis autocollimator. Similarly, if a yaw angle $\Delta\theta_y$ is applied to the grating reflector, it will generate the same amount of linear displacement on the detectors along the X-direction, which is also the same as the two-axis autocollimator. On the other hand, if a roll angle $\Delta\theta_z$ is applied to the grating reflector, the two first-order diffracted light spots will rotate about the zeroth-order diffracted light spot, which can be utilized for the detection of $\Delta\theta_z$.

Based on the results in Fig. 2.8, the three-axis angles $\Delta\theta_x$, $\Delta\theta_y$ and $\Delta\theta_z$ can be measured simultaneously by using the setup shown in Fig. 2.9 or that in Fig. 2.10. In Fig. 2.9, detectors A and B are used for detecting the displacements of the zeroth-order and one of the first-order diffracted beams. The two first-order diffracted beams are detected in Fig. 2.10 for the three-axis angle measurement.

Figure 2.11 shows a three-axis angle sensor based on the principle shown in Fig. 2.9 for detection of the angular error motion of a precision linear stage moving along the Z-axis. The magnitudes of the angular error motions are assumed to be small. A grating reflector is mounted on the stage moving table. The s-polarized light from a laser diode (LD) is collimated by a collimating lens (CL) and bent by a

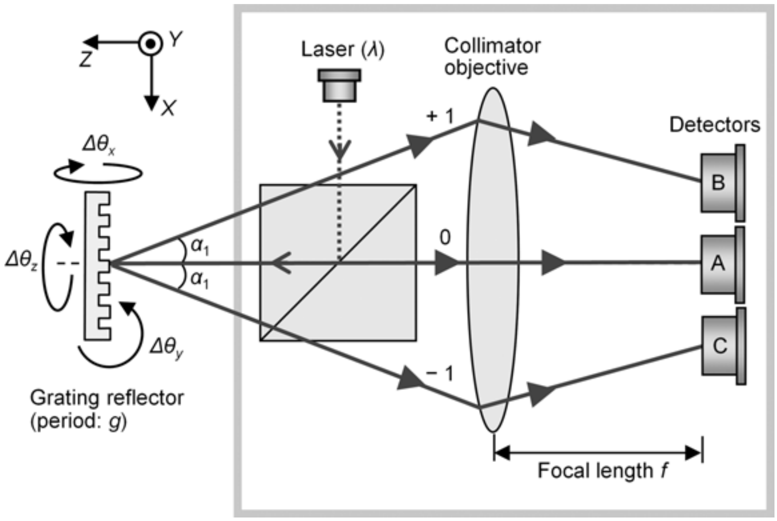

Fig. 2.7: Concept of the three-axis angle detection.

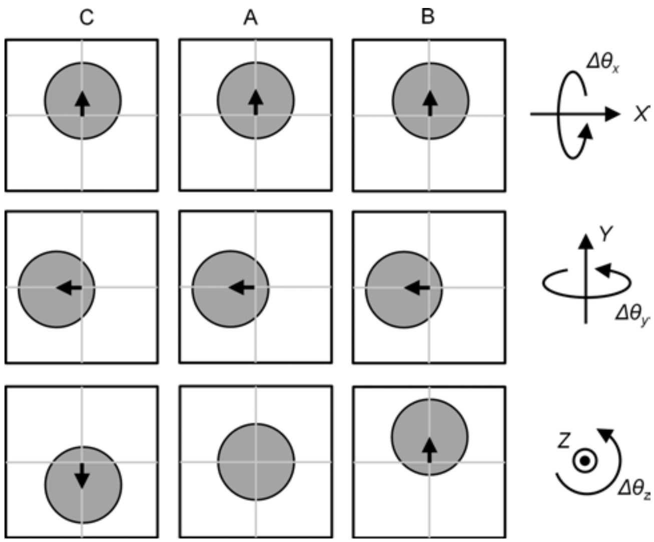

Fig. 2.8: Displacements of diffraction light spots on detectors for three-axis angle measurement.

polarizing beam splitter (PBS). The collimated light beam is then circularly polarized by a quarter-wave plate (QWP) before it is projected onto the grating reflector along the normal direction of the grating surface. The reflected zeroth-order and positive first-order diffracted beams from the grating reflector are converted into p-polarized beams by the QWP so that they can pass through the PBS to reach the

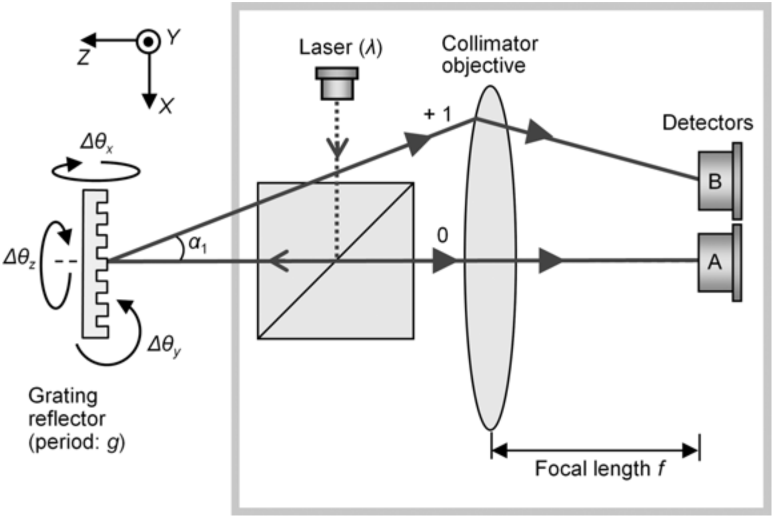

Fig. 2.9: Three-axis angle measurement by detecting zeroth-order and positive first-order diffracted beams.

autocollimation unit, which consists of a collimator objective and two-position sensing detectors. The two-position sensing detectors are located at the focal plane of the collimator objective to detect the X- and Y-directional displacements of the diffracted beam spots focused on detectors A and B. Since the distance between the sensor head and the grating reflector, which is called the working distance, varies with the position of the stage moving table, the three-axis angle sensor shown in Fig. 2.11 is referred to as the variable working distance type.

The displacements of the diffracted beam spots caused by the angular motion of the stage are shown in Fig. 2.12. A_0 and A_1 are the initial positions of the zeroth-order and the first-order diffracted beam spots, respectively. If the distance between A_0 and A_1 is denoted by L, L can be expressed by [13]

$$L = f \tan \alpha_1 \tag{2.1}$$

where f is the focal length of the collimator objective. α_1 is the diffraction angle of the first-order diffracted beam, which is given by [14]

$$\alpha_1 = \arcsin \frac{\lambda}{g} \tag{2.2}$$

where λ is the wavelength of the LD and g is the grating period of the grating reflector.

Assume that the first stage has a yaw error $\Delta\theta_y$, then a pitch error $\Delta\theta_x$, finally a roll error $\Delta\theta_z$ in sequence. In response to $\Delta\theta_y$, the zeroth-order and first-order

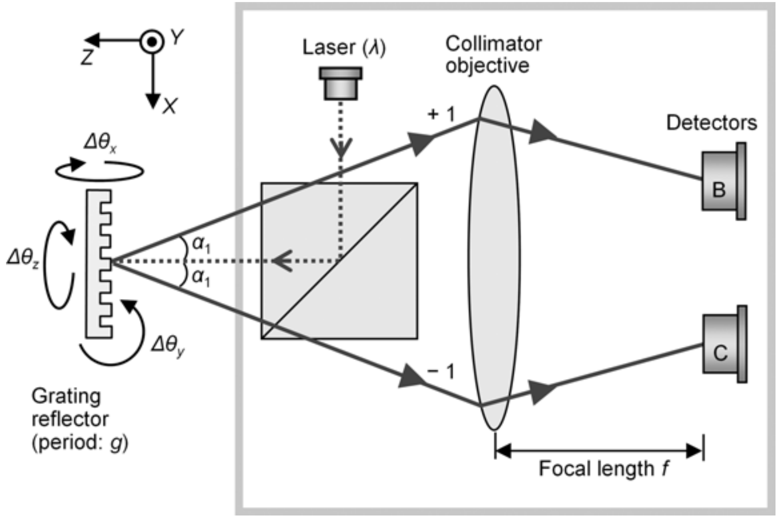

Fig. 2.10: Three-axis angle measurement by detecting positive and negative first-order diffracted beams.

diffracted beams will have the same angular deviations of $\Delta\theta_y$, which are converted into X-directional linear displacements of beam spots on the detectors by the collimator objective. As shown in Fig. 2.12, the zeroth-order and first-order diffracted beam spots move to B_0 and B_1 along the X-axis, respectively. Let the displacements of the beam spots be Δx_A and Δx_B, which are the X-directional outputs of Detector A and Detector B, respectively. Δx_A is equal to Δx_B. Because $\Delta\theta_y$ is small, it can be obtained by [13]:

$$\Delta\theta_y = \frac{\Delta x_B}{S_{\theta y}} \tag{2.3}$$

$$S_{\theta y} = 2f \tag{2.4}$$

where $S_{\theta y}$ is the conversion ratio of the angular motion $\Delta\theta_y$ to the linear displacement Δx_B with a unit of mm/rad.

Similarly, $\Delta\theta_x$ makes the zeroth-order diffracted beam spot move from B_0 to C_0 and the first-order diffracted beam spot from B_1 to C_1. In Fig. 2.12, Δy_A and Δy_{B1} are the displacements generated by $\Delta\theta_x$ along the Y-axis, which are the Y-directional outputs of detectors A and B, respectively. $\Delta\theta_x$ can be obtained by

$$\Delta\theta_y = \frac{\Delta y_A}{S_{\theta x}} \tag{2.5}$$

$$S_{\theta x} = 2f \tag{2.6}$$

where $S_{\theta x}$ is the conversion ratio of the angular motion $\Delta\theta_x$ to the linear displacement Δy_A with a unit of mm/rad.